POTSDAM-INSTITUT FÜR KLIMAFOLGENFORSCHUNG

Glacial Abrupt Climate Change as a Multiscale Phenomenon Resulting from Monostable Excitable Dynamics

KENO RIECHERS,[a,b] GEORG GOTTWALD,[c] AND NIKLAS BOERS[a,b,d]

[a] *Complexity Science, Potsdam Institute for Climate Impact Research, Potsdam, Germany*
[b] *Earth System Modelling–School of Engineering and Design, Technical University of Munich, Munich, Germany*
[c] *School of Mathematics and Statistics, University of Sydney, Sydney, New South Wales, Australia*
[d] *Global Systems Institute, Department of Mathematics, University of Exeter, Exeter, United Kingdom*

(Manuscript received 22 May 2023, in final form 30 November 2023, accepted 24 January 2024)

ABSTRACT: Paleoclimate proxies reveal abrupt transitions of the North Atlantic climate during past glacial intervals known as Dansgaard–Oeschger (DO) events. A central feature of DO events is a sudden warming of about 10°C in Greenland marking the beginning relatively mild phases termed interstadials. These exhibit gradual cooling over several hundred to a few thousand years until a final abrupt decline brings the temperatures back to cold stadial levels. As of now, the exact mechanism behind this millennial-scale variability remains inconclusive. Here, we propose an excitable model to explain Dansgaard–Oeschger cycles, where interstadials occur as noise-induced state-space excursions. Our model comprises the mutual multiscale interactions between four dynamical variables representing Arctic atmospheric temperatures, Nordic seas' temperatures and sea ice cover, and the Atlantic meridional overturning circulation. The model's atmosphere–ocean heat flux is moderated by the sea ice, which in turn is subject to large perturbations dynamically generated by fast-evolving intermittent noise. If supercritical, perturbations trigger interstadial-like state-space excursions during which all four model variables undergo qualitative changes that consistently resemble the signature of interstadials in corresponding proxy records. As a physical intermittent process generating the noise, we propose convective events in the ocean or atmospheric blocking events. Our model accurately reproduces the DO cycle shape, return times, and the dependence of the interstadial and stadial durations on the background conditions. In contrast with the prevailing understanding that DO variability is based on bistability in the underlying dynamics, we show that multiscale, monostable excitable dynamics provides a promising alternative to explain millennial-scale climate variability associated with DO events.

SIGNIFICANCE STATEMENT: Recent research has highlighted the risk that some Earth system components might undergo abrupt and qualitative change in response to global warming. Proxy records provide evidence for past abrupt climatic changes fundamentally proving the possibility for highly nonlinear state transitions in the climate system. Understanding the dynamics that drove past changes of this kind may help to assess the risk of future tipping events. Here, we propose a new mechanism for the repeated sudden warming events over Greenland that punctuated the last glacial's climate and reproduce the warmer interstadial intervals drawing on a multiscale, excitable conceptual climate model. Therein, the warmer intervals appear as state-space excursions following stochastic supercritical excitations caused by non-Gaussian noise, which is dynamically generated via fast intermittent dynamics.

KEYWORDS: North Atlantic Ocean; Paleoclimate; Dynamical system model; Nonlinear models

1. Introduction

Stable water isotope records from Greenland ice cores provide evidence for repeated abrupt climatic shifts during the last glacial interval. Decadal-scale transitions from low to high values of $\delta^{18}O$ (Fig. 1a) indicate sudden warming events at the drilling site, which are termed Dansgaard–Oeschger (DO) events (Dansgaard et al. 1982, 1984; Johnsen et al. 1992; Dansgaard et al. 1993; North Greenland Ice Core Project Members 2004). The temperature increases of approximately 5°–15°C (Jouzel et al. 1997; Johnsen et al. 2001; Landais et al. 2005; Huber et al. 2006; Kindler et al. 2014) were followed by phases of milder, yet moderately cooling temperatures called interstadials. Typically, a final and more abrupt decline brought the climate back to a colder state known as stadial climate. The millennial-scale successions of interstadials and stadials are often referred to as DO cycles.

The signature of DO cycles is found in numerous paleoclimatic proxy records around the globe, including speleothems and Antarctic ice cores (Voelker 2002; Menviel et al. 2020). These records show that the DO cycles were most pronounced in the North Atlantic region but were not limited to it. Instead, they seized several components of the global climate system. For instance, DO events are associated with large-scale reorganizations of the Northern Hemisphere atmospheric circulation (Ruth et al. 2007; Fischer et al. 2007; Schüpbach et al. 2018) including a northward shift of the ITCZ (Menviel et al. 2020) with strong impacts on the Asian and South American monsoon systems (Wang et al. 2001; Kanner et al. 2012; Cheng et al. 2013; Zhang et al. 2017; Corrick et al. 2020). Given the strong local impact, processes active in the North Atlantic region such as sea ice or deep water formation are believed to be central to the triggering mechanism

Corresponding author: Keno Riechers, riechers@pik-potsdam.de

DOI: 10.1175/JCLI-D-23-0308.1

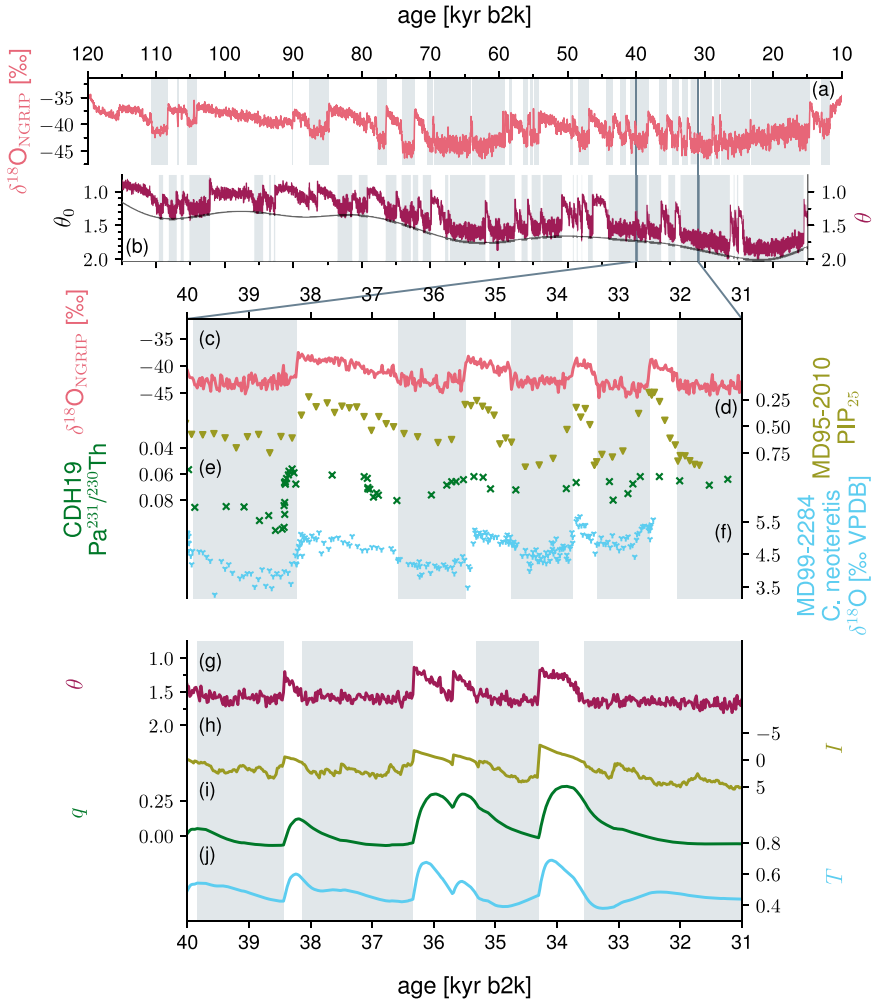

FIG. 1. Paleoclimatic proxy evidence for characteristic features of DO variability together with corresponding results of our model defined by Eqs. (1)–(7). (a) 20-yr mean NGRIP δ^{18}O data (Seierstad et al. 2014; Rasmussen et al. 2014) interpreted as a qualitative proxy of air temperatures over Greenland (data available at https://www.iceandclimate.nbi.ku.dk/data/, last access: 3 Mar 2023). (b) Simulated Arctic atmospheric air temperatures θ. (c) Zoom into the period 40–31 kyr b2k of (a); the period was chosen due to the availability of proxy data. (d) PIP_{25} index from the marine sediment core MD95-2010 (Sadatzki et al. 2020). The PIP_{25} index is indicative of past sea ice cover at the core site with values of 1 and 0 corresponding to perennial sea ice and open-ocean conditions, respectively. (e) Pa/Th ratios from the marine sediment core CDH19 from the Bermuda Rise as provided by Henry et al. (2016). The ratios are interpreted as a direct measure of the AMOC strength, with lower values corresponding to stronger overturning and vice versa. (f) δ^{18}O of the benthic species *C. neoteretis* (Dokken et al. 2013) shown on a revised age scale (Berben et al. 2020; Sadatzki et al. 2020). According to the most recent interpretation of the data, the benthic δ^{18}O is mostly indicative of past intermediate to deep-ocean temperatures (Ezat et al. 2014; Sadatzki et al. 2020), with higher values indicating colder temperatures and vice versa. (g)–(j) Corresponding model results: (g) the Arctic atmospheric temperature θ, (h) the Nordic seas' sea ice cover I, (i) the AMOC strength q, and (j) the Nordic seas intermediate to deep water temperatures T. The proxy records shown in (c)–(f) should be directly compared to the simulated trajectories shown in (g)–(j), respectively. All model variables are given in dimensionless values (see appendix).

of DO events (e.g., Dokken et al. 2013; Boers et al. 2018; Vettoretti and Peltier 2018; Menviel et al. 2020; Sadatzki et al. 2020).

To date there is no conclusive theory that fully explains the mechanism of DO cycles. Several climatic components have been proposed to be relevant, including ocean dynamics, atmospheric events, sea ice, ice sheets, and freshwater fluxes (Broecker et al. 1985; Ganopolski and Rahmstorf 2001; Petersen et al. 2013; Dokken et al. 2013; Zhang et al. 2014; Vettoretti and

Peltier 2018; Boers et al. 2018; Li and Born 2019). Similarly, several dynamic mechanisms have been invoked to explain the DO events, ranging from external drivers such as (periodically) changing freshwater fluxes (Ganopolski and Rahmstorf 2001; Timmermann et al. 2003; Menviel et al. 2014) and noise-induced transitions between two stable states (Ditlevsen 1999; Ditlevsen et al. 2005, 2007; Lohmann and Ditlevsen 2018; Lohmann and Svensson 2022) to dynamically self-generating mechanisms including self-sustained oscillations (Broecker et al. 1985, 1990; Rasmussen and Thomsen 2004; Dokken et al. 2013; Vettoretti and Peltier 2018; Boers et al. 2018; Vettoretti et al. 2022).

Building on the results of Gottwald (2021) we consider here a paradigm for DO variability which to date has received only a little attention. We present an excitable multiscale model for the dynamics of Greenlandic air temperatures, Arctic sea ice, the Nordic seas' intermediate to deep water temperatures and the strength of the Atlantic meridional overturning circulation (AMOC). For certain parameter values the model supports a single stable fixed point corresponding to stadial climate conditions. In response to sea ice perturbations above a critical threshold, the system takes prolonged excursions in state space. Along this excitation path, it passes through a region of slow transitive dynamics that can be identified with the interstadial climate state consistently in all four model dimensions. The required magnitude of the perturbations is generated by an intermittent non-Gaussian driving noise detailed later. A DO-like excitation mechanism for the North Atlantic glacial climate has previously been identified in an intermediate complexity model by Ganopolski and Rahmstorf (2002). Later, Vettoretti et al. (2022) showed in a conceptual framework that shorter interstadials could be explained as excitations. An important new aspect of our model is that it effectively translates the strength of the exciting noise pulse into the duration of the triggered interstadial therefore providing a possible explanation for the great variety of the real-world's interstadials in terms of shape and duration. Overall, the model reproduces the following five central aspects of DO cycles in an interpretable manner (cf. Fig. 1):

1) Shape of DO cycles: The characteristic shape of DO cycles in the NGRIP ice core $\delta^{18}O$ record, as described above, is comprised of an abrupt warming followed by a gradual cooling and final stage of accelerated cooling back to stadial climate conditions. On close inspection there are many deviations from this archetypical shape such as short temperature declines within interstadials and vice versa, rebound events shortly before interstadial–stadial transitions or continuous interstadial–stadial cooling transitions without accelerated cooling (cf. Figs. 1a,c).
2) Duration of stadials and interstadials: Both stadials and interstadials lasted from centuries to millennia. The ratio between interstadial and stadial duration, however, changed over time and was presumably influenced by external (orbital) forcing and internal forcing from the background climate state through the ice sheet configuration or atmospheric CO_2 concentrations (Rial and Saha 2011; Roberts and Saha 2017; Mitsui and Crucifix 2017; Lohmann and Ditlevsen 2018; Boers et al. 2018; Zhang et al. 2021; Kuniyoshi et al. 2022; Vettoretti et al. 2022). The early glacial (~115–71 kyr b2k) was dominated by long-lasting interstadials and relatively warm stadial conditions. The middle part of the glacial (~71–29 kyr b2k) was characterized by frequent DO events with intermediate-length stadials and interstadials. Finally, colder stadials and very short interstadials prevailed during the later part of the last glacial (~29–14 kyr b2k). Compare Fig. 1a and see Kindler et al. (2014) for temperature levels.
3) In-phase sea ice dynamics: Sea ice in the Nordic seas and the North Atlantic varied in phase with Greenland temperatures. During stadials an extensive sea ice cover prevailed, whereas interstadials exhibited conditions ranging from open water to seasonal sea ice cover (Li et al. 2005, 2010; Dokken et al. 2013; Hoff et al. 2016; Sadatzki et al. 2020) (cf. Fig. 1d).
4) Nordic seas' temperature inversion: Several studies report warming of the ice-covered stadial Nordic seas at intermediate and large depth caused by a continued inflow of warm water masses from the south (Rasmussen and Thomsen 2004; Ezat et al. 2014; Sadatzki et al. 2020) (cf. Fig. 1f). Near-surface water temperatures show a similar pattern with an additional warming flush in synchrony with DO events (Dokken et al. 2013). The oceanic heat—initially trapped under the sea ice—is hypothesized to have abruptly warmed the polar atmosphere in response to sudden sea ice retreat during DO events (e.g., Rial and Saha 2011; Dokken et al. 2013; Boers et al. 2018; Vettoretti and Peltier 2018; Kuniyoshi et al. 2022).
5) AMOC switches: Multiple lines of direct and indirect evidence, thoroughly summarized by Lynch-Stieglitz (2017), point to changes in the strength of the AMOC in phase with Greenland temperatures, with weak (or no) overturning during (Heinrich) stadials and stronger overturning during interstadials (cf. Fig. 1e). An active AMOC is typically believed to have provided the necessary northward heat transport to explain the milder Arctic climate during interstadials.

From a physical modeling point of view, the results presented below suggest that the DO events may have been caused by complex multiscale interactions between several climate subsystems acting on separate time scales: the ocean circulation, the sea ice, the large-scale atmosphere ordered from slow to fast characteristic time scales, and intermittent atmospheric or oceanic events on time scales faster than the sea ice time scale and comparable to the atmospheric time scale.

The paper is structured as follows: We introduce the model in section 2 and analyze its dynamics in section 3. We interpret the results in a physical context and also perform a detailed model–data comparison in terms of the above listed five key features. Section 4 discusses the results and relates them to previous research. We conclude in section 5 with a summary of our key findings.

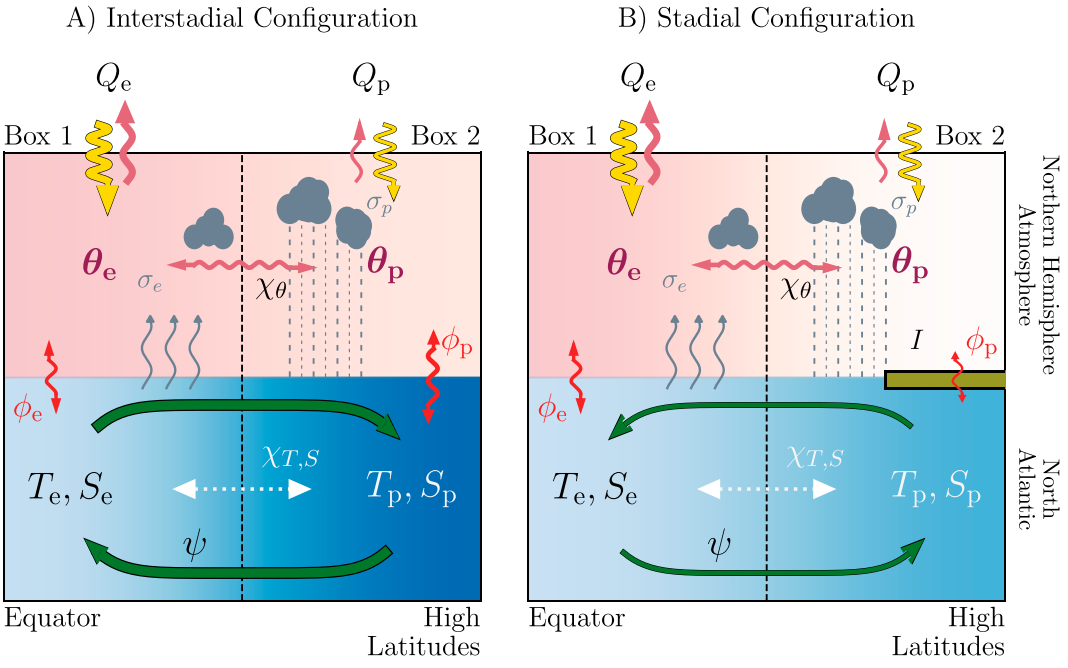

FIG. 2. Schematic illustration of the excitable monostable model used to reproduce DO variability of the last glacial. The three key model components are the North Atlantic (bottom), the Northern Hemisphere atmosphere in the North Atlantic region (upper part), and the sea ice in the Nordic seas (green bar on the right). Oceanic temperature and salinity in the equatorial and polar region are denoted as T_e, S_e, and T_p, S_p, respectively. The corresponding meridional gradients follow as $T = T_e - T_p$ and $S = S_e - S_p$. Analogously, the atmospheric temperature gradient $\theta = \theta_e - \theta_p$ is given by the difference between equatorial and polar atmospheric temperatures. The solar differential heating caused by the difference in the net radiative heat fluxes Q_e and Q_p together with the atmospheric diffusive flux χ_θ sets the background hemispheric meridional temperature gradient θ_0. Atmosphere and ocean exchange heat in both the equatorial and the polar region ($\phi_{e,p}$). The oceanic gradients T and S give rise to a meridional density gradient, that in turn drives the flow ψ, which represents the AMOC. On top of that, the diffusive fluxes $\chi_{T,S}$ counteract the existing gradients in the ocean. The oceanic salinity gradient S is maintained by constant freshwater fluxes $\sigma_{e,p}$ in the equatorial and polar regions, e.g., caused by a surplus of evaporation in the tropics and precipitation in the high latitudes illustrated in gray. (a) The interstadial configuration is characterized by the absence of sea ice in the high latitudes. This allows for an elevated heat flux ϕ_p resulting in a relatively cold ocean and a relatively warm atmosphere in the high latitudes. The pronounced meridional temperature gradient in the ocean yields a strong overturning flow ψ. (b) In the stadial configuration, the sea ice insulates ocean and atmosphere from one another. The sea-ice-covered high-latitude ocean is relatively warm and the atmosphere above it is cold. The reduction of the oceanic temperature gradient causes a weak and reversed overturning flow. The derivation of the model equations under consideration of the illustrated flows is presented in the appendix.

2. Methods

a. *Monostable excitable model of DO variability*

From the slowest to the fastest time scale, the key components of our conceptual multiscale model are: (i) the Atlantic Ocean represented by the meridional temperature and salinity gradients $T(t)$ and $S(t)$ between the equator and the Nordic seas, (ii) the Nordic seas' sea ice extent $I(t)$, (iii) the Northern Hemisphere atmosphere represented by the meridional temperature gradient $\theta(t)$, and (iv) intermittent oceanic and atmospheric anomalies ξ_t and regular Gaussian atmospheric fluctuations ζ_t. All variables are nondimensionalized by a suitable rescaling (see appendix). The model setup is schematically illustrated in Fig. 2. For the ease of notation, we will omit the explicit time dependency of the four dynamical variables in the following [i.e., we write θ instead of $\theta(t)$ for example]; fast driving noise processes will be subscripted with t. A detailed derivation of the individual model components is provided in the appendix. Here we give only a concise description of the model.

Following the classical Stommel model (Stommel 1961; Cessi 1994), on the slowest time scale τ_{ocean} the oceanic meridional gradients of temperature and salinity evolve according to

$$\tau_{\text{ocean}}\dot{T} = -\gamma(I)(T - \theta) - (1 + \mu|T - S|)T, \tag{1}$$

$$\tau_{\text{ocean}}\dot{S} = \sigma - (1 + \mu|T - S|)S, \tag{2}$$

and determine the strength of the density driven overturning flow

$$q = T - S, \tag{3}$$

which represents the AMOC strength. The ocean temperature T is coupled to the atmospheric temperature gradient θ

via a heat flux whose strength is moderated by the sea ice. This heat flux is effectively represented by the mutual relaxation rate $\gamma(I)$. The atmospheric meridional temperature gradient θ relaxes against two opposing temperature gradients, namely a prescribed background state θ_0 which is determined by the net radiative heat fluxes and the atmospheric diffusion and the oceanic gradient T:

$$\tau_{\text{atm}}\dot{\theta} = -\eta(\theta - \theta_0) - \gamma(I)(\theta - T) + \zeta_t. \tag{4}$$

Here, $\tau_{\text{atm}} < \tau_{\text{ocean}}$ is a fast atmospheric time scale and ζ_t denotes a Gaussian white noise process that disturbs the atmospheric dynamics. The ratio between the effective atmospheric relaxation rate η and the mutual atmosphere–ocean relaxation rate $\gamma(I)$ determines the influences of θ_0 and T on θ.

It is widely accepted that changing background climate conditions strongly influenced DO variability over the course of the last glacial (Rial and Saha 2011; Roberts and Saha 2017; Mitsui and Crucifix 2017; Boers et al. 2018). This effect is considered in our model by altering the atmospheric background state θ_0 over time according to

$$\theta_0(t) = 1.59 + 0.23\delta^{18}\text{O}^*_{\text{LR04}}(t). \tag{5}$$

The normalized benthic stable isotope data $\delta^{18}\text{O}^*_{\text{LR04}}(t)$ is indicative of past global ice volume changes (Lisiecki and Raymo 2005). We argue that a colder background climate increases the atmospheric background temperature gradient θ_0 due to Arctic amplification (Masson-Delmotte et al. 2006).

On an intermediate time scale τ_{ice} with $\tau_{\text{ocean}} > \tau_{\text{ice}} > \tau_{\text{atm}}$, the temporal evolution of the sea ice is given by the seasonally averaged Eisenman model (Eisenman 2012; Lohmann et al. 2021)

$$\tau_{\text{ice}}\dot{I} = \Delta\tanh\left(\frac{I}{h}\right) - R_0H(I)I - L_0 + L_1\theta - L_2I + \xi_t, \tag{6}$$

where $H(I)$ denotes the Heaviside function and the term $L_1\theta$ represents the influence of the atmosphere on the sea ice formation, with large atmospheric temperature gradients—i.e., colder temperatures at high northern latitudes—fostering sea ice growth and vice versa. We assume that the ocean's surface layer, which is not resolved in our box model, is dominated by atmospheric temperatures. This justifies the direct coupling of the sea ice to the atmosphere. The remaining terms represent the ice–albedo feedback, sea ice export, and the net incoming and outgoing radiation linearized with respect to I, respectively. For a detailed discussion of the sea ice model, please see the appendix. In the original model formulation, the nondimensionalized variable I represents the sea ice thickness over a horizontally homogeneous ocean column (Eisenman 2012). Therein, values of $I < 0$ correspond to an ice-free state. Here, we interpret I as a stylized representation of the annually averaged sea ice volume in the Nordic seas. The time scale $\tau_{\text{ice}} = 200$ years may be understood as the rate at which the multiyear sea ice front advances southward. The stochastic process ξ_t models fast intermittent random sea ice retreat events that will be explained in greater detail below.

The sea ice itself couples back to the ocean and atmosphere dynamics by acting as a dynamic insulator (Dokken et al. 2013; Boers et al. 2018) and modifying the respective mutual relaxation rate according to

$$\gamma(I) = \gamma_0 + \frac{\Delta\gamma}{2}\left\{\tanh\left[\frac{-(I - I_0)}{\omega}\right] + 1\right\}. \tag{7}$$

In the presence of a stadial sea ice cover ($I > 0.5$) the polar ocean is shielded from the atmosphere and the mutual heat flux is heavily suppressed. In contrast, a reduced interstadial sea ice cover yields a strong atmosphere–ocean heat flux and correspondingly a high mutual relaxation rate γ. The choice of I_0 determines what should be regarded as intermediate sea ice cover in our model. Values of the parameters used in our numerical simulation are summarized in Table 1.

The next paragraph establishes a correspondence between the model variables and the considered climate variables, or more precisely their respective proxy variables. Although T and θ are gradients, we may compare them directly with observations for oceanic and atmospheric temperature proxies from high northern latitudes, respectively, with larger gradients implying colder temperatures in the polar region. This is justified since the comparably much larger size of the equatorial region compared to the polar region implies substantially larger heat capacities for the considered equatorial boxes. We thus ascribe changes in the gradients mostly to changes in the polar regions and interpret T and θ as direct counterparts for intermediate and deep ocean temperature proxy records from the Nordic seas (cf. Fig. 1f with Fig. 1j; increases in the gradients reflect cooling of the polar boxes) and δ^{18}O records from Greenland ice cores (cf. Fig. 1c with Fig. 1h), respectively. The comparison of q with proxies for past AMOC strength is straightforward (cf. Fig. 1e with Fig. 1j) and so is the comparison of I with proxies for past sea ice extent (cf. Fig. 1d with Fig. 1i).

For the parameter configuration specified in Table 1 the deterministic model defined by Eqs. (1)–(4) and Eqs. (6) and (7) yields monostable dynamics for $\theta_0 > 1.275$. However, it also features a region of slow transitive dynamics located where the nullclines of the atmosphere and sea ice variables are closest (cf. Figs. 4a,f). We will show later that this metastable state in the model's state space can be identified with interstadial climate conditions of the North Atlantic region. To make this metastable state accessible to the dynamics, in the following, we introduce the noise processes ξ_t and ζ_t that mimic the effect of unresolved events occurring on time scales faster than the characteristic time scales τ_{ice} and τ_{atm} of the sea ice and atmosphere dynamics, respectively. Notice that both the monostability and the excitability depend on the specific choice of parameters. For other values, the dynamical features of the model may differ.

b. *Stochastic (intermittent) forcing processes ξ_t and ζ_t*

The atmosphere variable θ is assumed to be subjected to Gaussian white noise forcing $\zeta_t = \sigma_\theta\dot{W}$ with standard Brownian motion W. This noise can be motivated as the effective

TABLE 1. Model parameters used in all simulations unless stated otherwise. The parameters are chosen to reproduce the key features of DO events.

Parameter	Definition	Value
Time scales		
τ_{ocean}	Oceanic time scale in years	800
τ_{ice}	Sea ice time scale in years	200
τ_{atm}	Atmospheric time scale in years	0.6
Atmosphere–ocean model		
γ_0	Atmosphere–ocean relaxation rate at full sea ice cover	0.5
$\Delta\gamma$	Amplitude of the sea ice's insulation effect	3.5
H	Atmospheric heat dissipation rate	4
M	Flux parameter	7.5
Σ	Freshwater influx	0.7
Sea ice model		
L_0	Zeroth-order sea ice OLR	1.75
L_1	Linear dependence of sea ice OLR on the atmosphere	1.85
L_2	Linear dependence of sea ice OLR on the sea ice	0.35
Δ	Strength of sea ice albedo feedback	0.25
h	Characteristic sea ice albedo feedback scale	0.08
R_0	Rate of sea ice export	0.4
Ω	Characteristic insulation scale of sea ice	0.8
I_0	Sea ice value, at which half of the insulation effect is reached	−0.5

stochastic effect of unresolved strongly chaotic atmospheric fluctuations on θ (Hasselmann 1976). It does not substantially affect the dynamics of Eqs. (1)–(4) and Eqs. (6) and (7) but generates more realistic fluctuations of θ in accordance with the NGRIP δ^{18}O record.

The sea ice noise ξ_t, however, plays a crucial role in triggering DO events. To generate rare but large forcing events that allow the system to leave the stadial fixed point and enter the metastable state, non-Gaussian noise is required. Gottwald (2021) showed that α-stable noise, which is characterized by the occurrence of discrete jumps, can be dynamically generated in a multiscale setting to produce abrupt warming events in a Stommel model driven by a simple sea ice model. Here, we postulate that sea ice is subjected to rare and intermittent fast processes. According to the theory laid out in Gottwald and Melbourne (2013a,b), Gottwald et al. (2017), and Gottwald (2021), this forcing, when integrated, gives rise to an effective α-stable component in the resulting dynamics of the sea ice. The discrete jumps of the generated α-stable process represent large stochastic sea ice melting events.

By controlling the mutual relaxation rate $\gamma(I)$ the sea ice in turn drives the atmospheric and oceanic variables θ and T with emergent non-Gaussian noise. Indeed, signatures of non-Gaussian α-stable noise have been detected by Ditlevsen (1999) in the calcium concentration record of the GRIP ice core (Fuhrer et al. 1993).

We propose two possible physical mechanisms that may constitute such intermittent forcing on the sea ice: oceanic convective events and atmospheric anomalies. During stadials, the Nordic seas' sea ice is shielded from the warmer subsurface and deep waters by a thin layer of cold and fresh water (Dokken et al. 2013; Sadatzki et al. 2020). We hypothesize that intermittent convective events may temporarily remove this layer and melt sea ice from below, efficiently opening up polynya through which oceanic heat could be released to the atmosphere (Vettoretti and Peltier 2018). Either, after locally releasing sufficient heat, a stable stratification of the ocean reestablishes and the polynya refreeze, or the convective events might remove a critical amount of sea ice and push the system into the metastable interstadial state.

Strong atmospheric anomalies constitute another possible source of intermittent sea ice forcing. Kleppin et al. (2015) and Drijfhout et al. (2013) describe—although in a different setting—how persistent atmospheric anomalies can drive the high northern latitude climate into a substantially altered state. Storms or baroclinic instabilities could also act as initiators of oceanic convective events.

We postulate that the above-described mechanisms giving rise to intermittent anomalous forcing events are only active during stadials. During interstadials, we argue that convectively driven sea ice removal should not have a strong impact on the already northward displaced sea ice edge. Traveling northward the warm Atlantic inflow loses too much heat before it can be subducted under the sea ice. Thus, heat cannot efficiently accumulate underneath the sea ice which is a precondition for large convective sea ice removal. Similarly, we argue that atmospheric anomalous forcing events require a certain meridional temperature gradient and a stadial configuration of the jet stream (Li and Born 2019). Therefore, we impose a Gaussian white noise forcing of the sea ice dynamics with $\xi_t = \sigma_I \dot{W}$ with standard Brownian motion W if no pronounced stadial sea ice cover is present ($I < 0.5$). Since sea ice fluctuations are smaller, the smaller the sea ice extent, we choose relatively small σ_I as compared to the sea ice fluctuation emerging from the more complex stadial driving noise which we describe in the following.

To model intermittent convective events or atmospheric anomalies, we follow Gottwald and Melbourne (2013a,b) and design a (mean-zero) process that consists of a succession of turbulent and laminar periods. The forcing during the laminar periods is set to a constant $\xi_t = -c$ whereas during the turbulent periods it fluctuates around $\xi_t = c$ according to standard Brownian motion with $\xi_t = c + \sigma_{\text{tur}}\dot{W}$. The respective durations of these phases are themselves random variables. In particular, durations of the laminar period τ_{lam} can be arbitrarily long and are distributed according to a Pareto law:

$$\tau_{\text{lam}} \sim \frac{1}{\sigma_{\text{lam}}}\left[1 + k\left(\frac{\tau_{\text{lam}} - \mu_{\text{lam}}}{\sigma_{\text{lam}}}\right)\right]^{(-1/k+1)}, \tag{8}$$

with shape parameter $k = 1/\alpha$, scale parameter σ_{lam}, and location parameter $\mu_{\text{lam}} = \sigma_{\text{lam}}/k$. Hence, laminar periods last on average for $\mathbb{E}[\tau_{\text{lam}}] = \sigma_{\text{lam}}\alpha^2/(\alpha - 1)$ time units (assuming $\alpha > 1$). The durations of turbulent periods τ_{tur} are uniformly distributed around the mean $\overline{\tau}_{\text{tur}} = \mathbb{E}[\tau_{\text{lam}}]$ with $\tau_{\text{tur}} \sim \overline{\tau}_{\text{tur}} + U[-\overline{\tau}_{\text{tur}}/2, +\overline{\tau}_{\text{tur}}/2]$, where $U[a, b]$ denotes the uniform distribution between the limits a and b. When such a process is integrated, during the laminar periods we obtain ballistic flights with $\int_0^t \xi_s ds = -ct$. The heavy tail of the Pareto distribution assigns a probability of $(\alpha\sigma_{\text{lam}})^\alpha \tau^{-\alpha}$ to durations $\tau_{\text{lam}} > \tau$, and for $\alpha < 2$ allows for nonvanishing probabilities of ballistic flights of arbitrary lengths. This renders $\int \xi_t dt$ an effective α-stable process. This mechanism of intermittent laminar dynamics generating α-stable noise is illustrated in Fig. 3, where we show the stochastic process ξ_t and its integrated form.

Long-lasting laminar forcing events may remove large amounts of sea ice and thus entail an abrupt shift in the atmosphere–ocean heat flux, which determines the climatic state of the coupled atmosphere–ocean model (cf. Fig. 4). Such dynamically generated perturbations are capable of inducing metastable interstadial dynamics in our model as we will show in the next section. In Table 2 we list the parameters used to generate the noise.

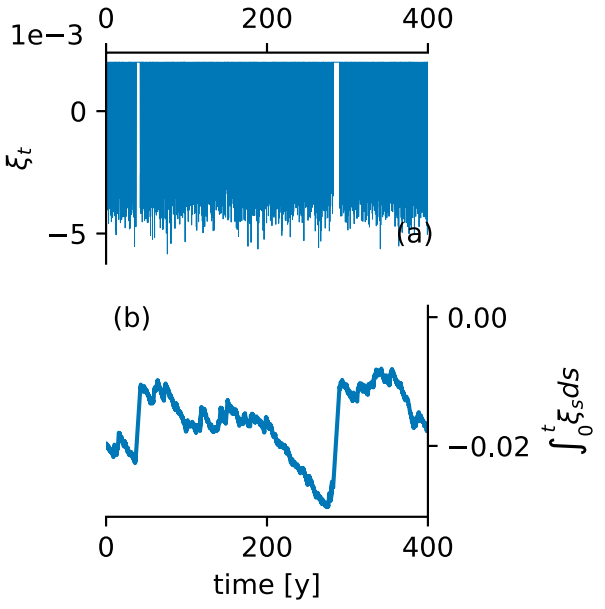

FIG. 3. Illustration of (a) the driving noise process ξ_t acting on the sea ice and its integrated form $\int_0^t \xi_s ds$ (b). It is clearly seen how prolonged laminar phases of the driving noise ξ_t result in jumps in the integrated $\int_0^t \xi_s ds$. These jumps may correspond to supercritical sea ice removals, which in turn trigger DO events in our excitable model.

3. Results

We first analyze the response of the deterministic coupled model to imposed perturbations of the sea ice cover with $\zeta_t = \xi_t = 0$ and a constant climate background temperature θ_0 in section 3a. We show that long lasting interstadial-like excursions occur as a consequence of supercritical sea ice perturbations of the stable stadial state. This phenomenon results from a complex interplay of the three separate time scales and the slow deterministic dynamics in a particular metastable region of the state space, which is characterized by high proximity of the θ and I nullclines (cf. Fig. 4).

In section 3b we show that the intermittent noise ξ_t is capable of generating such supercritical perturbations to the sea ice acting as triggers of interstadials. Finally, the full stochastic model, coupled to the background climate, is run over the entire last glacial in section 3c.

Notice that in this section, we use the term *nullcline* in slight deviation from its formal definition. Formally, the *nullcline* of any of the model's variables is the set of points in the four-dimensional state space where its derivative is zero. Let $\Omega = (\theta, T, q)$ denote the state of the atmosphere–ocean model component of the coupled model. Conditioned on a given value for the sea ice, the atmosphere–ocean model has either one or three fixed points in the subspace spanned by θ, T and q. For ease of notation, we refer to the set $\{(\theta, I)\colon d\Omega/dt = 0\}$ as the θ-nullcline in the θ–I plane (T- and q-nullclines are defined correspondingly). Since the temporal evolution of sea ice only depends on θ, the I-nullcline shall be defined as the set of points where $dI/dt = 0$ in the θ–I plane.

a. *Deterministic response to sea ice perturbations*

To understand how our model may explain DO variability, we investigate how the deterministic system given by Eqs. (1)–(4) and Eqs. (6) and (7) with $\zeta_t = 0$, $\xi_t = 0$ recovers after large imposed perturbations of the sea ice variable. We consider two different choices of $\theta_0 = 1.3$ and $\theta_0 = 1.6$, corresponding to warm and intermediate glacial climate backgrounds, respectively (Fig. 4). In simulations initialized in the stadial stable state, at time $t_p = 200$ years, the sea ice is abruptly removed by manually setting $I(t) = I_p$ with $I_p = \{0.2, 0, -0.2, -0.5, -1, -2\}$. Subsequently we let the system evolve freely and relax back to the unique stadial fixed point. The character of the relaxation depends on the strength of the perturbation and on the value of the climate background θ_0. In general, in the warmer background climate with $\theta_0 = 1.3$, the sea ice nullcline and the

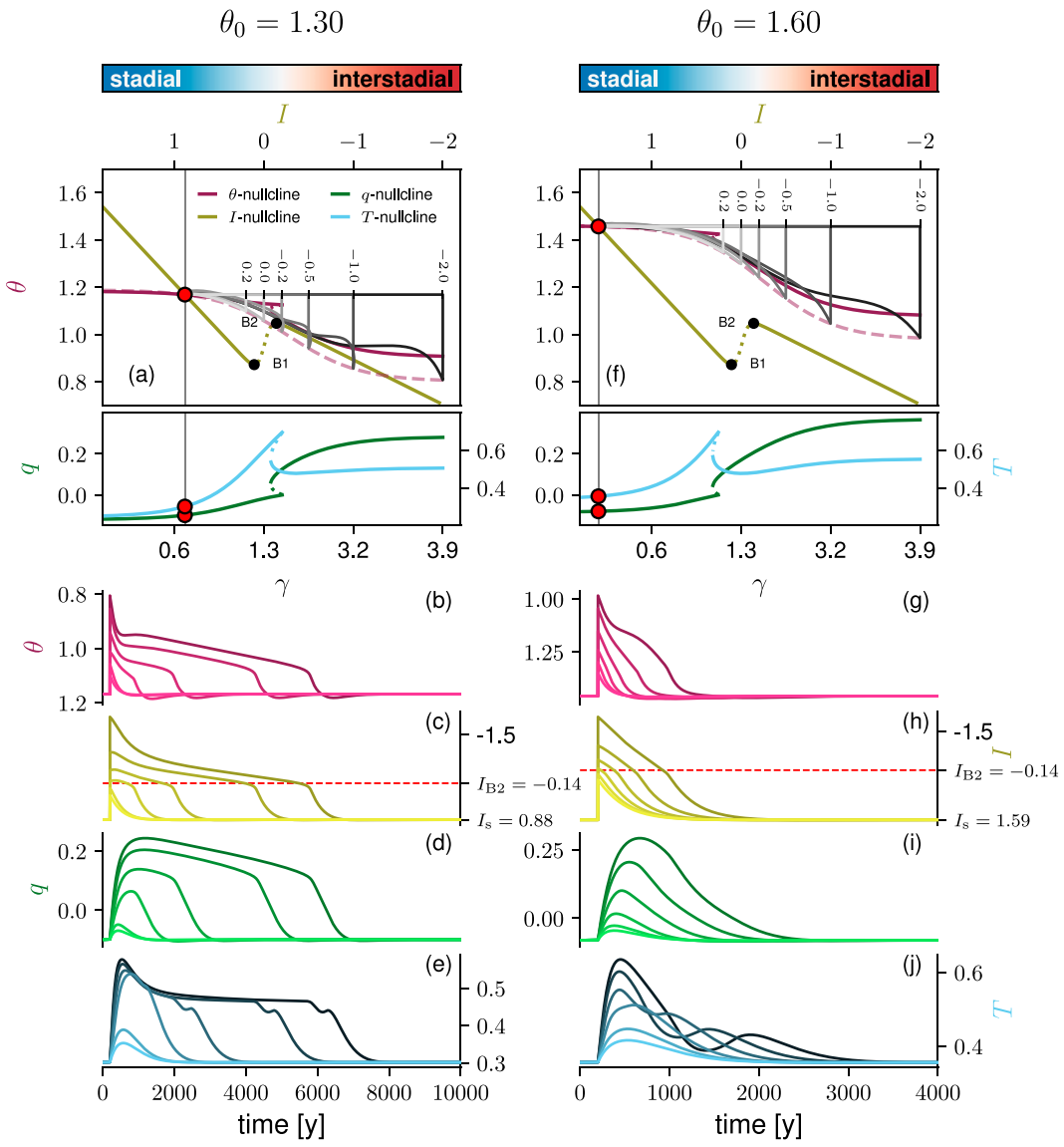

FIG. 4. Trajectories of the deterministic system defined by Eqs. (1)–(7) initialized in the stable state and subjected to instantaneous sea ice retreat at $t = 200$ with $\zeta_t = \xi_t = 0$. Six different sea ice perturbations have been applied: $I_p = \{0.2, 0.0, -0.2, -0.5, -1.0, -2.0\}$ [gray horizontal lines in (a) and (f)]. Results are shown for (a)–(e) warmer ($\theta_0 = 1.3$) and (f)–(j) colder ($\theta_0 = 1.6$) background climate. The plots in (a) and (f) show the trajectories in the θ–I plane together with the corresponding nullclines of all four model variables. A prescribed value for the sea ice variable (top axis) determines the atmosphere–ocean relaxation rate $\gamma(I)$ (bottom axis), which in turn sets the stable fixed points for the coupled atmosphere–ocean model comprising θ, T, and q. Strong sea ice cover and a low mutual relaxation rate yield a cold polar atmosphere (large θ), warm intermediate and deep waters in the Nordic seas (small T) and a weak AMOC (small $|q|$). This configuration corresponds to stadial climate conditions as inferred from proxy records. A small sea ice cover reversely entails a warm polar atmosphere (small θ), cold Nordic seas (large T) and an active AMOC (large $|q|$), which can be identified with interstadial climate conditions. Since only θ couples back to the sea ice I, intersections of the I- and θ-nullcline constitute fixed points of the entire system in the θ–I plane with values for T and q (red dots) following from the heat exchange rate associated with this intersection. The remaining panels show the trajectories of the individual system variables against time for the different sea ice perturbations with darker colors corresponding to stronger sea ice removal. The horizontal dashed lines in (c) and (h) mark the critical sea ice threshold I_{B2}, which constitutes the highest possible sea ice cover in the low-ice regime. Similarly, the sea ice bifurcation point I_{B1} marks the lowest possible sea ice cover in an ice-rich regime viewed in the θ–I plane.

TABLE 2. Parameters for the stochastic processes ζ_t and ξ_t that drive the atmosphere and sea ice in Eqs. (4) and (6), respectively.

Parameter	Definition	Value
Atmospheric noise ζ_t		
σ_θ	Amplitude of the atmospheric noise	0.04
Sea ice noise ξ_t during stadials		
c	Laminar forcing strength	0.2
σ_{tur}	Amplitude of the Brownian motion during turbulent phase	0.01
$k = 1/\alpha$	Shape parameter of Pareto distribution	0.62
σ_{lam}	Scale parameter of the Pareto distribution	2
$\mu_{\text{lam}} = \sigma_{\text{lam}}/k$	Location parameter of the Pareto distribution	3.2
Sea ice noise ξ_t during interstadials		
σ_I	Amplitude of interstadial Brownian motion	0.006

atmosphere nullcline are much closer together (cf. Fig. 4). This allows for pronounced interstadials, resembling real-world interstadials from the early glacial. For intermediate background climate ($\theta_0 = 1.6$) the distance between the two nullclines is larger. This yields shorter interstadials similar to those observed during the midglacials. We observe the following distinct phases in the system response.

Phase A: Immediate atmospheric response. Over short time intervals the slow ocean dynamics T and S can be considered as constants for the faster atmosphere dynamics θ. Hence, the atmospheric temperature gradient rapidly decreases (i.e., the Arctic temperature increases) to the value θ_p (see Figs. 4b,g), which is approximately given as the solution to $\gamma(I_p)(\theta_p - T_s) + \eta(\theta_p - \theta_0) = 0$ (shown as a light dashed line in Figs. 4a,f as a guide to the eye). The subscript s denotes the respective stadial fixed point values. Physically, θ_p is determined by a new balance between the competing influences of θ_0 and of T_s. Suddenly exposed to the warm stadial ocean (small T) that was previously shielded from the atmosphere by the stadial sea ice cover, the high-latitude atmosphere now takes up much more oceanic heat. The slow model time scale τ_{ocean} may in this context be interpreted as the large heat capacity of the Nordic seas, allowing heat release to the atmosphere while their own temperature T remains unchanged on fast time scales.

Phase B: System-wide relaxation. We now discuss how the system relaxes form the perturbed state (θ_p, T_s, q_s, I_p) back to the unique stable fixed point (θ_s, T_s, q_s, I_s). Notice that the sea ice bifurcation point I_{B2} marks the lowest sea ice cover of the sea ice nullcline's stable branch with reduced sea ice cover (cf. Fig. 4). The relaxation is qualitatively different depending on whether the perturbation brings the sea ice to the low-ice regime ($I_p < I_{\text{B2}}$) or not. If that is the case, the system takes a prolonged excursion in state space with a two-stage relaxation process, of which the first stage can be identified with interstadial climate conditions. We call this scenario, which involves responses of all model variables, the supercritical case. If $I_p > I_{\text{B2}}$, then the system shows a straight relaxation back to stadial conditions without any substantial response of the oceanic variables to the initial perturbation. We term this scenario the subcritical case. The existence of both subcritical perturbations that rapidly relax back to the steady state and supercritical perturbations that cause long transitory dynamics back toward the steady state involving several time scales is a hallmark of so-called excitable media often found in neurophysiological systems (FitzHugh 1961; Nagumo et al. 1962).

Phase B: Subcritical case $I_p > I_{\text{B2}}$. In the subcritical case the system remains in an ice-rich state which due to the albedo feedback facilitates a fast regrowth of the sea ice. Consequently, the dynamics of I and θ jointly relax back straight to the stadial equilibrium as the regrowing sea ice increasingly shields the atmosphere from the warm stadial ocean. The oceanic variables on the other hand show hardly any response due to their higher inertia and the fast sea ice recovery. Qualitatively the general system response to subcritical perturbations is the same for $\theta_0 = 1.3$ and for $\theta_0 = 1.6$.

Phase B: Supercritical case $I_p < I_{\text{B2}}$—Stage 1. In contrast, in the supercritical case a phase of slowed-downed sea ice recovery occurs, giving the oceanic variables enough time to respond to the perturbation such that all model variables temporarily assume interstadial configurations, i.e., in addition to the elevated Arctic atmospheric temperature (low gradient θ) and the reduced Nordic seas' ice cover (low I), the AMOC assumes its strong circulation mode (large q) and the Nordic seas cool at intermediate and large depth (high gradient T) in agreement with proxy evidence (cf. Fig. 1).

As a consequence of the substantially reduced sea ice cover the ice–albedo feedback now inhibits the reformation of the sea ice and in the presence of warm atmospheric conditions θ_p the sea ice regrows at a slow rate toward I_{B2} or retreats even farther if the perturbed state is located left of the sea ice nullcline in the θ–I plane (cf. Fig. 4a). As the atmosphere continuously dissipates the heat it receives from the ocean while relaxing toward θ_0, the ocean starts to notably cool (increase in T). In turn, the oceanic cooling reduces the atmospheric uptake of oceanic heat and as a result the Arctic atmosphere simultaneously cools (see the pronounced increase in θ in Figs. 4b,g shortly after the perturbations). This effect inevitably prevents a stabilization of the system in the low-ice regime and ensures that the sea ice eventually regrows. A second consequence of the Nordic seas' cooling is the transition of the AMOC from a salinity-driven weak mode to the temperature-driven strong mode. This completes the interstadial configuration of the four model variables and allows us to

identify this first stage of the supercritical relaxation with the interstadial climate. Fully reactivated, the AMOC's northward oceanic heat transport stabilizes the temperatures of the Nordic seas and over the course of the remaining interstadial the slow adjustments of the other variables are driven by the incremental sea ice regrowth.

The nature and duration of the interstadial stage depend on both the size of the initial sea ice perturbation I_p and the closeness of the sea ice nullcline and the atmosphere nullcline. If the two nullclines are close (as for $\theta_0 = 1.3$) the dynamics of θ and I is comparably slow (cf. the dynamics for $\theta_0 = 1.3$ in Fig. 4). Sufficiently strong sea ice perturbations then result in pronounced interstadials during which all system variables hardly change over an extended period of time. If the nullclines are farther apart (as for $\theta_0 = 1.60$) the interstadial state is less pronounced and characterized by a gradual change in all model variables, driven by steady sea ice regrowth. The separation of the atmospheric and sea ice nullcline is how the conceptual model captures the effects of the background climate state.

Phase B: supercritical case $I_p < I_{B2}$—Stage 2. Once the sea ice has regrown past I_{B2}, its further regrowth accelerates substantially, marking the beginning of the second stage in the supercritical system-wide relaxation process. This is due to the strongly changing albedo effect around intermediate sea ice cover. The regrowing sea ice increasingly prevents oceanic heat loss to the atmosphere, which entails polar atmospheric cooling and initiates warming of the Nordic seas. The reduction of the oceanic temperature gradient is closely followed by a corresponding reduction in the AMOC strength. Since the atmosphere equilibrates quasi-adiabatically to the declining mutual relaxation rate $\gamma(I)$, it cools at the same accelerated rate as the ice recovers and both atmosphere and sea ice reach stadial configuration within a few hundred years after the sea ice passed its threshold I_{B2}. The oceanic variables follow with some inertia; they exhibit a sustained relaxation after the faster atmosphere and sea ice have already clearly transitioned to their stadial configuration. This second stage of the supercritical relaxation process corresponds to the abrupt interstadial–stadial transitions observed in the paleoclimate record.

b. *Noise-driven interstadials*

We now show that the intermittent driving noise ξ_t is able to generate supercritical sea ice perturbations capable of triggering DO events. Figure 5 shows trajectories of the dynamics determined by Eqs. (1)–(4) and Eqs. (6) and (7) under the influence of the driving noises ξ_t and ζ_t with a constant atmospheric background climatic state θ_0. Overall, there is high visual agreement between simulated θ trajectories (Fig. 5) and the DO cycles recorded in the NGRIP δ^{18}O data (Figs. 1a,c).

For $\theta_0 = 1.3$, the θ-trajectory resembles DO cycles from the early glacial, with persistent interstadials separated by short stadials. For $\theta_0 = 1.6$ the θ-trajectory has a greater similarity with the mid- to late glacial, with shorter interstadials and predominantly stadial conditions. Confirming the discussion in the previous section, interstadials last longer and have a more pronounced plateau in all variables for the smaller atmospheric background temperature gradient $\theta_0 = 1.3$. Moreover, an increase in the stadial duration can be observed for larger θ_0. The colder stadial conditions associated with larger θ_0 imply an increased distance between the sea ice's stable stadial configuration I_s and the critical sea ice threshold I_{B2}. Hence, for unchanged driving noise ξ_t, the probability for the noise to drive the system across I_{B2} is reduced for larger θ_0 and thus the waiting time between two supercritical stochastic forcing events is higher and the stadials are longer. However, this effect is attenuated by the fact that DO events can also be triggered by two pronounced yet subcritical laminar forcing periods in quick succession.

The Gaussian atmospheric noise process ζ_t driving the θ variable blurs the exact timing of DO cooling transitions in agreement with δ^{18}O ice core records. In the sea ice, however, these transitions are still fairly distinct. Compared to the deterministic setup, sea ice perturbations of the same strength yield shorter interstadials. Indeed, small sea ice fluctuations can disrupt the delicate balance of influences that yields the slow sea ice regrowth of the metastable interstadial and may easily push the system across the critical threshold of I_{B2}. This initiates the final stage of accelerated sea ice regrowth which ends the interstadial.

Remarkably, our model reproduces several observed irregular features of the δ^{18}O record, with respect to variability in terms of shape, duration, and amplitude of DO cycles. The different strengths of the sea ice perturbations translate into different lengths of the interstadial intervals for given background conditions θ_0. In agreement with the NGRIP δ^{18}O record, the shorter interstadials in the simulation with a colder background climate ($\theta_0 = 1.6$) lack a clear two-stage cooling. Instead, θ transitions back to the stadial state more continuously compared to the longer interstadials simulated with warmer a background climate of $\theta_0 = 1.3$. Both trajectories exhibit pronounced perturbations within stadials toward a warmer Arctic atmosphere that do not develop into a full interstadial. Perturbations of this kind can also be found in the NGRIP record [cf. for example interstadials 5.1, 16.2, and 21.2 in Rasmussen et al. (2014)].

c. *Realistic climate background*

Finally, we run a simulation of the last glacial with the full model defined by Eqs. (1)–(7) with a realistically changing atmospheric background climate according to Eq. (5) (cf. Fig. 1b). Including the temporal variations of the climate background conditions aligns the simulated stadial and interstadial durations with those observed in the NGRIP records. The resulting θ trajectory shows excellent agreement with the NGRIP δ^{18}O record.

With the linear coupling to the LR04 δ^{18}O stack introduced in Eq. (5) the atmospheric background state θ_0 assumes low values around 1.3 during the early parts of the last glacial and increases to high values $\theta_0 > 1.9$ around the last glacial maximum. As shown in sections 3a and 3b, this leads to longer lasting interstadials during the early glacial and shorter ones during the late glacial, with the opposite effect although much less pronounced for stadials. Hence, the predominance of long-lasting interstadials with only short stadial inceptions in

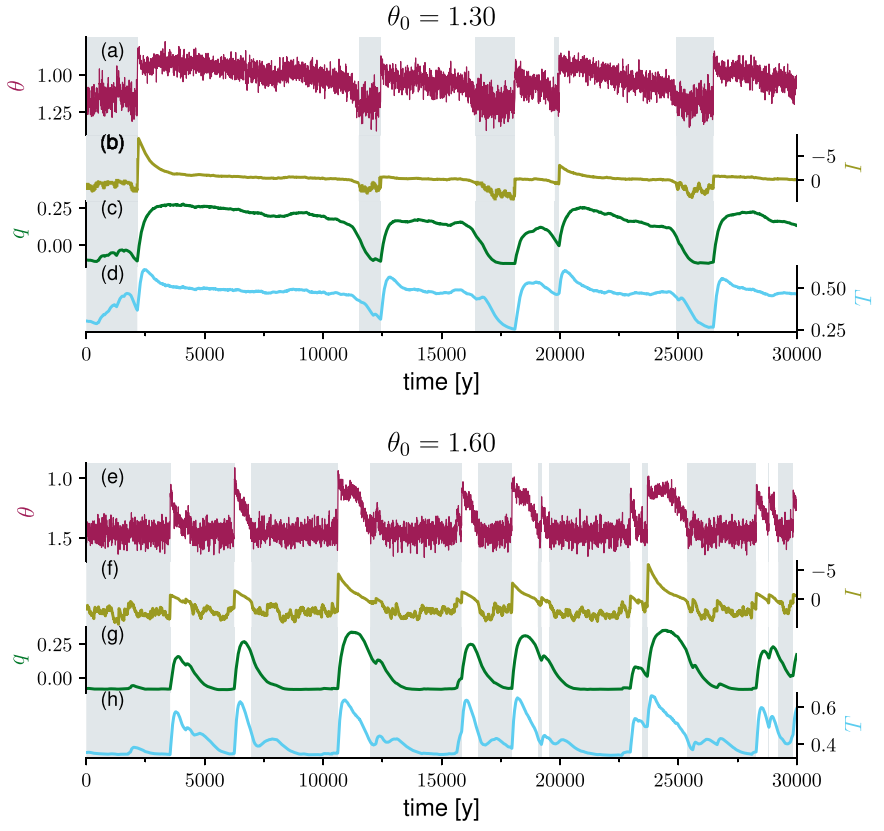

FIG. 5. Trajectories of the model system defined by Eqs. (1)–(7) driven by the noise scheme as described in section 2b, i.e., with nonzero noise ζ_t and ξ_t, for (a)–(d) $\theta_0 = 1.3$ and (e)–(h) $\theta_0 = 1.6$. The gray shading indicates stadial intervals. A DO event is defined by at least 25 consecutive years of sea ice cover $I > I_{B2}$ within a stadial followed by at least 15 years of reduced sea ice cover of $I < I_{B2}$. Provided that the system is in an interstadial state, the reverse interstadial–stadial transition occurs when the sea ice regrows past $I_c = 0.5$ and maintains this level in an average over the following 25 years. The hysteresis in the definition of climate transitions prevents a jumping back and forth between the two states when the sea ice fluctuates close to a potential critical threshold and gives rise to well-defined climatic periods.

the early glacial is reversed toward the late glacial (cf. Fig. 6). In general, the time scales of the stadials and interstadials match those observed in the proxy data throughout the entire last glacial. During the very cold conditions toward the end of the last glacial, DO events are unlikely but not impossible to occur in our simulations.

4. Discussion

Overall, the modeled atmospheric temperature θ qualitatively resembles the NGRIP δ^{18}O record over the entire last glacial in terms of shape and periodicity of DO cycles (cf. Fig. 1a with Fig. 1b). The general features of strong (reduced) sea ice cover, weak (strong) AMOC and warm (cold) Nordic seas during stadials (interstadials) are likewise consistently reproduced by the model (cf. Figs. 1c–f with Figs. 1g–j).

In principle, the dimensionless units of our model could be translated into physical units by multiplication with the corresponding scaling factors (see appendix). However, since proxies themselves mainly provide qualitative information on the past we focus on the qualitative analysis of our model. Above all, we aim to demonstrate a plausible mechanism for DO cycles and place less emphasis on quantitative accuracy. Nonetheless, it should be mentioned that multiplying the simulated atmospheric warming of $\Delta\theta \sim 0.4$ with a characteristic atmospheric gradient of $\theta_* \sim 25$°C used for the nondimensionalization yields realistic DO warming amplitudes of 10°C.

We now discuss the similarity between proxy records and our simulations with focus on the five key characteristics of DO variability as listed in the introduction, which rely on a multitude of marine, cryosphere, and terrestrial proxy records (Rasmussen et al. 1996b; Rasmussen and Thomsen 2004; Dokken et al. 2013; Ezat et al. 2014; Hoff et al. 2016; Lynch-Stieglitz 2017; Menviel et al. 2020; Sadatzki et al. 2020).

1) Shape of DO cycles: The general shape of the DO cycles is well reproduced by the atmospheric temperature θ (Figs. 1a,c vs Figs. 1b,g). Our model further resolves

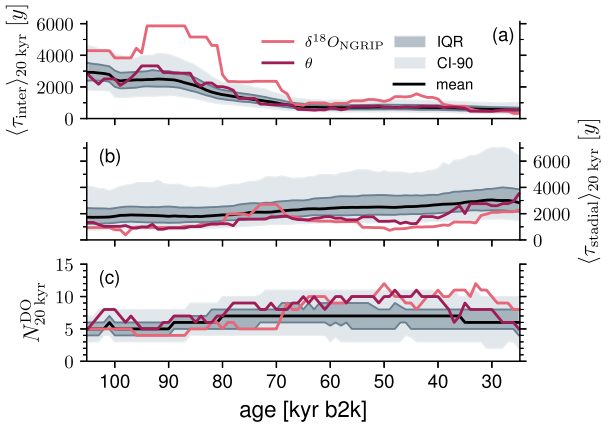

FIG. 6. The effect of the changing θ_0 on the interstadial and stadial durations. (a) The average duration of all interstadials inside running windows of 20 kyr centered on the respective point in time ($\langle\tau_{inter}\rangle_{20kyr}$) for the proxy data (rose) and the simulation (wine) together with corresponding mean (black line), interquartile range (IQR; dark gray) and 90% credibility interval (CI-90; light gray) computed from 1000 model runs. The 20-kyr mean duration takes into account all interstadials that are either fully included in the window or that end or start within the window. Interstadials that stretch across the window boundaries are considered with their full duration. (b) As in (a), but for the 20-kyr running-mean duration of stadials ($\langle\tau_{inter}\rangle_{20kyr}$). (c) Number of DO events occurring in a 20-kyr running-window N^{DO}_{20kyr} with the same color coding as before.

several finer-scale features of the proxy record of the last glacial, such as precursor events: short-lived strong positive excursions in the $\delta^{18}O$ data that do not evolve into full interstadials such as the interstadial 5.1 at ~31 kyr b2k or the interstadial 16.2 at ~58 kyr b2k or very short stadial inceptions similar to the stadial 23.1 at ~90 kyr b2k and the stadial 21.2 at ~85 kyr b2k that yield apparent back-to-back interstadials (Rasmussen et al. 2014; cf. Figs. 1b and 5). Furthermore, consistent with the proxy record, several interstadials exhibit a continuous trend of moderate cooling back to full stadial conditions instead of the more typical abrupt final cooling [cf. for example interstadials 5.2, 8, and 10 in Rasmussen et al. (2014)]. The slow variations in the overall stadial and interstadial levels are reproduced by our simulations, however with an apparent mismatch prior to the last glacial maximum, where the NGRIP $\delta^{18}O$ record shows a persistent warming trend (within a stadial climate), while our simulation evolves to colder temperatures (cf. Fig. 6). This discrepancy is caused by the fact that, in contrast to the local warming trend observed in the NGRIP record, the LR04 $\delta^{18}O$, which drives the background climate of our model, indicates a global cooling trend prior to the last glacial maximum (Clark et al. 2009). Potentially, this discrepancy could be circumvented by coupling θ_0 to orbital parameters instead of the background climate.

2) Duration of stadials and interstadials: The modeled variability of stadial and interstadial durations is in good agreement with the data (cf. Fig. 6). In our simulations the coupling of the background climate θ_0 to the LR04 benthic $\delta^{18}O$ introduced in Eq. (5) causes a gradual transition from a predominantly interstadial to a predominantly stadial climate across the last glacial due to the mechanisms explained in sections 3b and 3c. In the early glacial, our model does not generate sufficiently long interstadials. This could be circumvented by adjusting the background climate such that the interstadial state is weakly stable during this time interval. However, this would come at the cost that simulated interstadials would no longer show a cooling trend. Between 50 and 40 kyr b2k our model generates slightly too few DO events resulting in a too-high stadial duration.
3) In-phase sea ice dynamics: The extensive (reduced) sea ice cover during stadials (interstadials) suggested by proxy records (Dokken et al. 2013; Hoff et al. 2016; Sadatzki et al. 2019, 2020) is well reproduced by our model; the sea ice I consistently regrows at a moderate rate over the course of the interstadial, before it returns to its stadial extent in a final phase of accelerated regrowth marking the interstadial–stadial transition. Overall, this behavior agrees with the sea ice dynamics in the Nordic seas across DO cycles as inferred by Sadatzki et al. (2020) and others (Dokken et al. 2013; Ezat et al. 2014; Hoff et al. 2016). While proxy records suggest a continued sea ice growth during the early stadial, the modeled sea ice I reaches its stadial extent already during the interstadial–stadial transition and the regrowth thus does not stretch significantly into the stadial phase.
4) Nordic seas' temperature inversion: In our interpretation of the modeled oceanic temperature gradient T, we ignore surface waters and regard T as an indicator of subsurface and deep water temperatures. Indeed, our model simulates warm Nordic seas at full stadial conditions (Fig. 1j), in line with the proxy records (Rasmussen and Thomsen 2004; Dokken et al. 2013; Ezat et al. 2014). At the beginning of interstadials, pronounced cooling sets in, which can be interpreted as a continuous convection-driven release of the heat previously stored underneath the sea ice cover. Approximately one-third into an interstadial the subsurface cooling is reversed into a gentler yet persistent warming trend caused by regrowing sea ice and decreasing heat loss, which accelerates across the transition back to stadial conditions, but is sustained in the subsequent stadial. In general, this pattern agrees very well with existing paleoclimate proxies (Rasmussen and Thomsen 2004; Dokken et al. 2013; Ezat et al. 2014; Sadatzki et al. 2020, cf. Fig. 1f). The moderate warming that persists over the final two thirds of the interstadial can be observed in a very similar manner in the benthic $\delta^{18}O$ from marine sediment cores indicative of deep ocean temperatures (cf. Figs. 1f and 1j). The deep ocean warming is attributed to a gradual reduction of deep convection over the course of the interstadial driven by regrowing sea ice (Sadatzki et al. 2020; Ezat et al. 2014). The observed sustained warming of the intermediate and deep ocean into stadials is reproduced by our model, where a salinity-driven stadial AMOC ($q < 0$) counteracts an existing meridional temperature gradient and the sea ice cover prevents heat loss to the atmosphere.

5) AMOC switches: The correspondence between strong (weak) overturning and interstadial (stadial) climate conditions is widely accepted (Broecker et al. 1985; Ganopolski and Rahmstorf 2001; Lynch-Stieglitz 2017; Henry et al. 2016; Gottschalk et al. 2015; Vettoretti and Peltier 2018; Menviel et al. 2020). However, the limited quality of the proxy data prevents a more detailed assessment of the changes in the AMOC during the course of a typical DO cycle (Henry et al. 2016; Lynch-Stieglitz 2017). It seems that the AMOC almost stopped during Heinrich stadials, while during non-Heinrich stadials it probably operated in a weak and shallow mode (Lynch-Stieglitz 2017). An AMOC reinvigoration is reported to have happened in synchrony with abrupt Greenland warmings, within the limits of dating uncertainties (Lynch-Stieglitz 2017). In general terms, simulated changes of the AMOC strength agree with this pattern apart from the specific expression of Heinrich events, which are not explicitly targeted by our modeling setup (cf. Figs. 1e,i). From the interstadial onset onward the AMOC strength increases until it plateaus somewhere halfway through the interstadial. Thereafter, a weakening trend sets in the strength of which is related to the climate background conditions and which stretches well into the stadial before the AMOC reassumes its stadial state.

   Notice that in the stable stadial state of the model, the AMOC is in fact negative (i.e., its flow is reversed with respect to the modern AMOC). Certainly, a complete reversal of the real AMOC seems unphysical. This could be circumvented by heuristically adding a constant positive offset to the AMOC strength representing, for example, a wind-driven component (Vettoretti et al. 2022). However, summarizing earlier findings Rasmussen and Thomsen (2004) pointed out that the flow across the Iceland–Scotland ridge may in fact have been reversed between stadials and interstadials. The initially unintended feature of the Stommel model could, in fact, reflect a real physical mechanism.

In summary, our four-dimensional model defined by Eqs. (1)–(7) reproduces central features of DO variability in terms of Arctic temperatures θ, Nordic seas' sea ice cover I, intermediate-to-deep water temperatures T, and the meridional overturning strength q. In particular, our modeling results align well with the characteristics of DO variability inferred from the study of marine sediment cores from the northern North Atlantic and the Nordic seas. First pointed out by Rasmussen et al. (1996b,a) a sustained inflow of North Atlantic warm water into the Nordic seas during stadial periods was later confirmed and integrated in a conceptual explanation for the emergence of DO variability by Rasmussen and Thomsen (2004): The sustained inflow of warm and salty waters during stadials is subducted under a strong halocline that eventually separates a cold and fresh surface layer from the intermediate and deep waters. These experience a gradual warming up to the point where the growing vertical temperature gradient destabilizes the stratification and (re)initiates deep convection. This in turn reinvigorates the AMOC and cools the intermediate to deep waters in the Nordic seas. The transition back to the stadials is more or less explicitly attributed to the prevailing glacial climate background conditions (Rasmussen and Thomsen 2004). Dokken et al. (2013) and later Sadatzki et al. (2020) supplemented this framework by providing observational evidence for extended (reduced) Nordic seas' ice cover during stadials (interstadials), highlighting the role of the sea ice as an insulator between atmosphere and ocean. Our model shows excellent agreement with corresponding proxy evidence (cf. Fig. 1) and integrates well into the above narrative. The insulating effect of the sea ice, which has previously also been considered by Boers et al. (2018) as a crucial component, is modeled explicitly in our study and is confirmed to be key to the changes between stadial and interstadial climates. It is worth mentioning that previous studies based on conceptual and intermediate complexity models instead leveraged changes (or perturbations) in the freshwater forcing as DO triggers instead of sudden shifts in the atmosphere–ocean heat flux (e.g., Ganopolski and Rahmstorf 2001, 2002; Timmermann et al. 2003; Menviel et al. 2014; Roberts and Saha 2017). The observed sustained stadial inflow of warm North Atlantic waters into the intermediate depth Nordic seas corresponds to a weak, salinity-driven AMOC in our model.

Importantly, in our model interstadials do correspond to metastable states that inevitably decay back to stadial climate conditions. This excitation mechanism previously investigated by Ganopolski and Rahmstorf (2002) and Vettoretti et al. (2022) adds an alternative view on DO cycles complementing the more common concepts based on either bistability or limit-cycle behavior (Ditlevsen 1999; Timmermann and Lohmann 2000; Ditlevsen et al. 2005; Livina et al. 2010; Rial and Saha 2011; Kwasniok 2013; Mitsui and Crucifix 2017; Roberts and Saha 2017; Lohmann and Ditlevsen 2019). Our model does not resolve the exact triggering mechanism and instead relies on intermittent noise, which may trigger DO events by removing sufficiently large amounts of sea ice reactivating atmosphere–ocean interaction in the high latitudes. So far, as a source of this noise, we have proposed either convective events in the ocean inspired by Sadatzki et al. (2020), Dokken et al. (2013), Rasmussen and Thomsen (2004), and Vettoretti and Peltier (2018) or atmospheric anomalies as described by Kleppin et al. (2015) and Li and Born (2019). The interplay of both mechanisms, as suggested by Sadatzki et al. (2020), might even be better suited to justify the choice of our driving noise.

Apart from its central role as the DO event trigger, we find that the driving intermittent process can explain specific details of the NGRIP δ^{18}O record. The variable strength of the supercritical perturbations generates variability in terms of the shape and the duration of interstadials similar to the observations. Similarly, the randomly distributed waiting times between supercritical perturbations control the variability of stadial durations. The stochastic nature of the DO trigger naturally allows for the reproduction of very short interstadials and back-to-back interstadials, which lack an extended stadial separating them. Furthermore, subcritical forcing events contribute to the observed larger fluctuations of the stadial Arctic atmospheric temperatures compared to those during interstadials. Subcritical events could be interpreted as weaker local convective events that only entail partial and temporary

removal of stadial sea ice with limited released of oceanic heat. In summary, we find a purely deterministic mechanism of DO events to be more difficult to reconcile with the variability of interstadial shapes in the proxy records.

It should be noted that the presence of the three different time scales τ_{ocean}, τ_{ice}, and τ_{atm} is crucial to obtain agreement between the modeled and the observed shape and duration of DO cycles. In particular, the relatively slow time scale of the sea ice is required to obtain sufficiently long interstadials. The other key ingredient for the successful simulation of sustained interstadial intervals is the proximity of the θ and ice nullclines, which gives rise to an additional dynamics-induced slow time scale and a metastable state. The existence of such a metastable state, whose expression is highly sensitive to background conditions, seems physically plausible in view of a delicate interplay between northward oceanic heat transport, the high latitude atmospheric temperatures and the ice-albedo feedback. The direct influence of warm Atlantic surface inflow in the Nordic seas on the formation of sea ice during interstadials has so far been neglected in our model, but should be considered in further research.

We acknowledge that the Stommel model represents the AMOC in a drastically simplified manner that misses important aspects like the AMOC's previously mentioned dependence on wind forcing (e.g., Yang et al. 2016; Weijer et al. 2019) or the relation between the AMOC strength and the pycnocline depth (Gnanadesikan 1999; De Boer et al. 2010; Nikurashin and Vallis 2011). It also neglects the coupling of the AMOC to other ocean basins and in particular the Southern Ocean, whose role in the DO variability was emphasized by Hines et al. (2019) and Thompson et al. (2019).

Recent simulations with comprehensive climate models were able to reproduce DO-like climate oscillations (Malmierca-Vallet et al. 2023, and references therein). These simulations do consistently reproduce the in-phase sea ice dynamics, the Nordic seas' temperature inversion and the AMOC switches as evident from the paleoclimate record and to a higher or lesser degree the general sawtooth shape of the Greenland temperatures over the course of one cycle. However, these simulations are run under constant background climate conditions and generally produce fairly stable DO cycle periods. They do not recover the large degree of variability of cycle durations and shapes observed in the NGRIP $\delta^{18}O$ record.

Targeted experiments have shown that orbital parameters, CO_2 concentration and ice sheet heights affect the cycle period (Zhang et al. 2021; Kuniyoshi et al. 2022; Vettoretti et al. 2022). However, it seems unclear if these models could reproduce the full spectrum of DO cycle variability in terms of amplitude, period, and shape in a transient simulation with changing ice sheets, orbital parameters, and CO_2. Here, our study may serve as a motivation to investigate why comprehensive climate models produce so regular DO cycles. According to our model, the key ingredient for generating irregular DO cycles is the stochastic sea ice dynamics, which is driven by an intermittent process. It might be worthwhile exploring if the models in question underestimate sea ice variability and if this leads to too stable DO cycles.

5. Conclusions

In summary, we have modeled DO cycles across the last glacial period as state-space excursions of an excitable monostable system, resolving the ocean, sea ice and atmosphere on increasingly fast time scales. DO events are triggered by a stochastic intermittent process that acts on the stadial sea ice cover. The associated effect on the atmospheric Arctic temperatures θ is consistent with the observed α-stable noise signature in the GRIP calcium record (Ditlevsen 1999). We propose as potential sources for the driving intermittent noise local and temporary convective instabilities in the stadial stratification of the Nordic seas (Singh et al. 2014; Jensen et al. 2016), persistent atmospheric anomalies (Kleppin et al. 2015; Li and Born 2019), or combinations thereof (Sadatzki et al. 2020). Our model reproduces several central aspects of the observed DO cycle patterns of four climate variables central to the physics of DO cycles: the typical saw-tooth shape of Arctic atmospheric temperatures (Johnsen et al. 2001; North Greenland Ice Core Project Members 2004), the reduced (extended) sea ice cover during interstadials (stadials) (Sadatzki et al. 2020, 2019; Hoff et al. 2016; Dokken et al. 2013), the strong interstadial AMOC, with sustained northward heat transport during stadials at a weaker level (Rasmussen et al. 1996b; Rasmussen and Thomsen 2004; Dokken et al. 2013; Henry et al. 2016; Lynch-Stieglitz 2017), and the corresponding stadial warming of the Nordic seas (Sadatzki et al. 2020; Dokken et al. 2013; Ezat et al. 2014; Rasmussen and Thomsen 2004). Furthermore, detailed aspects of the NGRIP $\delta^{18}O$ record, such as the variability of the interstadial shape and duration, higher-amplitude stadial fluctuations, and very short interstadials (stadials) during the colder (warmer) parts of the late glacial, are reproduced.

We summarize the most important features of our model that provide plausible mechanistic explanations to the last glacial's millennial-scale climate variability:

1) The intensity of ocean–atmosphere heat flux in the high northern latitudes is decisive for the state of the North Atlantic climate system. The heat flux is controlled by the sea ice.
2) Stochastic removal of the sea ice may abruptly expose the atmosphere to the influence of a large oceanic heat reservoir, causing abrupt atmospheric warming and oceanic cooling facilitated by reactivated deep convection. The oceanic cooling happens at a much slower rate due to the ocean's much larger heat capacity.
3) If sea ice is absent the oceanic heat loss to the atmosphere yields a strong meridional oceanic temperature gradient which in turn drives the AMOC's strong circulation mode.
4) In the interstadial configuration the North Atlantic climate system is only approximately close to an equilibrium state. Generally prevailing cold atmospheric temperatures in the high latitudes entail sea ice regrowth, which inevitably drives the system back to the stadial state.
5) The persistence of the interstadial state is highly sensitive to the background conditions.
6) The time-scale separation between ocean, sea ice, and atmosphere (from slow to fast) is central to the characteristic shape of Greenland interstadials in terms of Greenland temperature changes.

7) DO events are stochastically triggered by a random asymmetric intermittent process, mimicking abrupt large sea ice removal events.

We hope that our findings provide a helpful conceptual framework for further investigation of DO variability. We suggest testing the formulated excitability mechanism in comprehensive climate models by forced removal of sea ice. In that context, it could also be tested if stronger sea ice perturbations give rise to longer interstadials in comprehensive models as suggested by our model. Finally, it seems worthwhile to investigate the sea ice fluctuations in those models that successfully reproduce DO cycles and check if their statistics exhibit fat tails in the duration of reduced sea ice extent.

Acknowledgments. This is TiPES contribution #215; the TiPES ("Tipping Points in the Earth System") project has received funding from the European Union's Horizon 2020 research and innovation programme under grant agreement 820970. NB acknowledges further funding by the Volkswagen Foundation, the European Union's Horizon 2020 research and innovation programme under the Marie Sklodowska-Curie grant agreement 956170, and from the German Federal Ministry of Education and Research under Grant 01LS2001A.

Data availability statement. All data used for this study are publicly available. Data sources are indicated in the captions of the figures displaying the data. All code used to generate the presented results is available from https://zenodo.org/doi/10.5281/zenodo.10829868 or from https://github.com/kriechers/jcliD230308 together. External research data necessary to produce the figures are also included in the repository.

APPENDIX

Detailed Derivation of the Deterministic Part of the Model

a. Extended Stommel model

The starting point of our model derivation is the classical Stommel model (Stommel 1961; Cessi 1994). This model treats the North Atlantic ocean as two separate well-mixed boxes, each being characterized by a temperature $T_{e,p}$ and a salinity $S_{e,p}$. Here the indices e and p refer to the *equatorial* and *polar* box, respectively. In the classical Stommel model, the temperatures in the oceanic boxes relax toward prescribed temperatures of the atmosphere above. Here, we explicitly take into account a response of the atmospheric temperatures $\theta_{e,p}$ to the heat fluxes between atmosphere and ocean and correspondingly treat $\theta_{e,p}$ as dynamical variables. Figure 2 shows a schematic illustration of the model.

The atmosphere is exposed to net differential heating $Q_{e,p}$ caused by radiative imbalance between equatorial and polar regions. The diffusive meridional fluxes

$$\chi_\theta = \gamma_\theta(\theta_e - \theta_p), \quad \chi_T = \gamma_T(T_e - T_p), \quad \text{and} \quad \chi_S = \gamma_S(S_e - S_p) \tag{A1}$$

counteract existing temperature and salinity gradients in both the ocean and the atmosphere, respectively. The effective heat diffusivities γ_θ and γ_T are given in watts per kelvin, so that $\chi_{\theta,T}$ denotes a total heat flux across the boundary between the boxes. Similarly, γ_S is given in kilograms per second per PSU so that again, the flux χ_S denotes an effective flux of salt.

The atmosphere–ocean heat flux

$$\phi_{e,p} = \gamma_{e,p}(\theta_{e,p} - T_{e,p}) \quad \text{with} \quad \gamma_{e,p} \propto A_{e,p} \tag{A2}$$

is likewise assumed to be proportional to the corresponding temperature difference between the atmosphere and ocean. The flux parameters $\gamma_{e,p}$ are proportional to the corresponding atmosphere–ocean interface surfaces A_e and A_p. The salinities in the oceanic boxes are forced by an effective freshwater flux $\sigma_{e,p}$ caused by an imbalance between relatively stronger evaporation over the tropics and elevated precipitation and river runoff in the polar region. A meridional density gradient $\Delta\rho = \rho_e - \rho_p$ controlled by the oceanic temperature and salinity gradients between equator and pole drives an additional overturning flow

$$\psi = k\Delta\rho \tag{A3}$$

that represents the AMOC in this simple model. The flux parameter k relates the overturning strength to the density gradient.

These considerations lead to the following set of equations:

$$\dot{\theta}_e = \frac{1}{\lambda_e}\Big(Q_e - \gamma_e(\theta_e - T_e) - \gamma_\theta(\theta_e - \theta_p)\Big), \tag{A4a}$$

$$\dot{\theta}_p = \frac{1}{\lambda_p}\Big(Q_p - \gamma_p(\theta_p - T_p) + \gamma_\theta(\theta_e - \theta_p)\Big), \tag{A4b}$$

$$\dot{T}_e = \frac{1}{\Lambda_e}\Big(\gamma_e[\theta_e - T_e] - \gamma_T[T_e - T_p]\Big) - \frac{1}{V_p}k|\Delta\rho|(T_e - T_p), \tag{A4c}$$

$$\dot{T}_p = \frac{1}{\Lambda_p}\Big(\gamma_p[\theta_p - T_p] + \gamma_T[T_e - T_p]\Big) + \frac{1}{V_e}k|\Delta\rho|(T_e - T_p), \tag{A4d}$$

$$\dot{S}_e = \frac{1}{V_e}\Big(\sigma_e - \gamma_S(S_e - S_p) - k|\Delta\rho|[S_e - S_p]\Big), \tag{A4e}$$

$$\dot{S}_p = \frac{1}{V_p}\Big(\sigma_p + \gamma_S(S_e - S_p) + k|\Delta\rho|[S_e - S_p]\Big), \tag{A4f}$$

where the heat capacities of the ocean boxes $\Lambda_{e,p} = c_0\rho_0 V_{e,p}$ are given by the product of the specific heat capacity c_0, a reference density ρ_T, and the box volume $V_{e,p}$ (analogously for the atmospheric heat capacities $\lambda_{e,p} = c_\theta\rho_\theta W_{e,p}$, with $W_{e,p}$ denoting the atmospheric box volume). The overturning flow ψ enters these equations with an absolute value, because the direction of the flow is irrelevant for the exchange of heat and salt between the oceanic boxes.

Introducing the meridional gradients $X = X_e - X_p$ (e.g., $\theta = \theta_e - \theta_p$), the equations of motion can be reformulated as follows:

$$\begin{aligned}\frac{d\theta}{dt} &= \frac{\lambda_p Q_e - \lambda_e Q_p}{\lambda_e \lambda_p} - \frac{\gamma_e}{\lambda_e}(\theta_e - T_e) + \frac{\gamma_p}{\lambda_p}(\theta_p - T_p) - \gamma_\theta \frac{\lambda_p + \lambda_e}{\lambda_e \lambda_p}\theta \\ &= \frac{\lambda_p Q_e - \lambda_e Q_p}{\lambda_e \lambda_p} - \frac{\gamma_e}{\lambda_e}(\theta_e - T_e) + \frac{\gamma_p}{\lambda_p}(\theta - T - \theta_e + T_e) - \gamma_\theta \frac{\lambda_p + \lambda_e}{\lambda_e \lambda_p}\theta \\ &= \frac{\lambda_p Q_e - \lambda_e Q_p}{\lambda_e \lambda_p} - \frac{\gamma_e \lambda_p + \gamma_p \lambda_e}{\lambda_e \lambda_p}(\theta_e - T_e) + \frac{\gamma_p}{\lambda_p}(\theta - T) - \gamma_\theta \frac{\lambda_p + \lambda_e}{\lambda_e \lambda_p}\theta \\ &\approx -\frac{\gamma_\theta}{\lambda_p}(\theta - \theta_0) - \frac{\gamma_p}{\lambda_p}(\theta - T) + \frac{\gamma_e \lambda_p + \gamma_p \lambda_e}{\lambda_e \lambda_p}(\theta_e - T_e), \end{aligned} \tag{A5a}$$

$$\begin{aligned}\frac{dT}{dt} &= \frac{\gamma_e}{\Lambda_e}(\theta_e - T_e) - \frac{\gamma_p}{\Lambda_p}(\theta_p - T_p) - \frac{\Lambda_e + \Lambda_p}{\Lambda_e \Lambda_p}\gamma_T T - \frac{V_e + V_p}{V_e V_p} k|\Delta\rho| T \\ &= \frac{\gamma_e}{\Lambda_e}(\theta_e - T_e) - \frac{\gamma_p}{\Lambda_p}(\theta - T - \theta_e + T_e) - \frac{\Lambda_e + \Lambda_p}{\Lambda_e \Lambda_p}\gamma_T T - \frac{V_e + V_p}{V_e V_p} k|\Delta\rho| T \\ &= \frac{\Lambda_e \gamma_p + \Lambda_p \gamma_e}{\Lambda_e \Lambda_p}(\theta_e - T_e) - \frac{\gamma_p}{\Lambda_p}(\theta - T) - \frac{\Lambda_e + \Lambda_p}{\Lambda_e \Lambda_p}\gamma_T T - \frac{V_e + V_p}{V_e V_p} k|\Delta\rho| T \\ &\approx -\frac{\gamma_p}{\Lambda_p}(\theta - T) - \left(\frac{\gamma_T}{\Lambda_p} - \frac{k|\Delta\rho|}{V_p}\right) T + \frac{\Lambda_e \gamma_p + \Lambda_p \gamma_e}{\Lambda_e \Lambda_p}(\theta_e - T_e), \end{aligned} \tag{A5b}$$

$$\begin{aligned}\frac{dS}{dt} &= \frac{V_p \sigma_e + V_e \sigma_p}{V_e V_p} - \frac{V_e + V_p}{V_e V_p}(\gamma_S - k|\Delta\rho|) S \\ &\approx \frac{V_p \sigma_e + V_e \sigma_p}{V_e V_p} - \frac{1}{V_p}(\gamma_S - k|\Delta\rho|) S, \end{aligned} \tag{A5c}$$

with $\theta_0 = (\lambda_p/\gamma_\theta)[(\lambda_p Q_e - \lambda_e Q_p)/(\lambda_e \lambda_p)]$. Here, we have used the fact that $W_e \gg W_p$ and $V_e \gg V_p$, which implies $\lambda_e \gg \lambda_p$ and $\Lambda_e \gg \Lambda_p$.

Following Stommel (1961) we express the oceanic densities in terms of a linearized equation of state

$$\rho_{e,p} = \rho_0(1 - \alpha_T T_{e,p} + \beta_S S_{e,p}), \tag{A6a}$$

$$\Delta\rho = \rho_0(\beta_S S - \alpha_T T), \tag{A6b}$$

with the reference density $\rho_0 = 1029\ \mathrm{kg\ m^{-3}}$ and the thermal expansion and haline contraction coefficients $\alpha_T = 0.17 \times 10^{-3}\ \mathrm{K^{-1}}$ and $\beta_S = 0.75 \times 10^{-3}\ \mathrm{psu^{-1}}$, respectively.

We assume that the equatorial atmosphere and ocean are close to a thermal equilibrium with respect to each other with $\theta_e \sim T_e$. This allows us to neglect contributions of the form $[\theta_e - T_e]$. After rescaling all temperatures and the salinity according to

$$T' = \frac{T}{\theta_*}, \quad \theta' = \frac{\theta}{\theta_*}, \quad \theta'_0 = \frac{\theta_0}{\theta_*} = \mathcal{O}(1) \quad \text{and} \quad S' = \beta_S S/\alpha_T \theta_*, \tag{A7}$$

with $\theta_* = 25°\mathrm{C}$ denoting a typical atmospheric meridional temperature gradient, the equations of motion simplify to

$$\frac{d\theta'}{dt} \approx -\frac{\gamma_\theta}{\lambda_p}(\theta' - \theta'_0) - \frac{\gamma_p}{\lambda_p}(\theta' - T'), \tag{A8a}$$

$$\frac{dT'}{dt} \approx -\frac{\gamma_p}{\Lambda_p}(\theta' - T') - \left(\frac{\gamma_T}{\Lambda_p} - \frac{k\rho_0 \alpha_T \theta_*}{V_p}|S' - T'|\right) T', \tag{A8b}$$

$$\frac{dS'}{dt} \approx \frac{V_p \sigma_e + V_e \sigma_p}{V_e V_p}\frac{\beta_S}{\alpha_T \theta_*} - \left(\frac{\gamma_S}{V_p} - \frac{k\rho_0 \alpha_T \theta_*}{V_p}|S' - T'|\right) S'. \tag{A8c}$$

Since neither θ_* nor σ_{eff} depends on time in our model and since the meridional fluxes χ_θ and χ_T impact the polar boxes much more strongly than the equatorial boxes according to their respective heat capacities, temporal changes in the gradients are governed by changes in the polar quantities.

According to Cessi (1994), we interpret the quantities $\gamma_\theta/\lambda_p = \tau_\theta^{-1}$, $\gamma_p/\Lambda_p = \tau_r^{-1}$, $\gamma_T/\Lambda_p = \tau_d^{-1}$, and $k\rho_0 \alpha_T \theta_*/V_p = \tau_a^{-1}$ as the time scales of atmospheric diffusion, the relaxation of the oceanic temperatures toward the atmospheric ones, the oceanic horizontal diffusion and the oceanic advection, respectively. Some formulations of the Stommel model rely on two separate time scales for heat and salt diffusion (e.g., Lohmann and Ditlevsen 2019). However, following Stommel (1961) and

Cessi (1994) we assume that the time scale of haline diffusion with $\gamma_S/V_p = \tau_S^{-1}$ is the same as that of oceanic heat diffusion $\tau_S = \tau_d$, and therefore associated with turbulent diffusion. Multiplying all equations with the ocean diffusion time scale τ_d and omitting the primes yields

$$\tau_d \frac{d\theta}{dt} \approx -\frac{\tau_d}{\tau_\theta}(\theta - \theta_0) - \frac{\tau_d}{\tau_r}\frac{\Lambda_p}{\lambda_p}(\theta - T), \tag{A9a}$$

$$\tau_d \frac{dT}{dt} \approx -\frac{\tau_d}{\tau_r}(\theta - T) - \left(1 - \frac{\tau_d}{\tau_a}|S - T|\right)T, \tag{A9b}$$

$$\tau_d \frac{dS}{dt} \approx \sigma_{\text{eff}} - \left(1 - \frac{\tau_d}{\tau_a}|S - T|\right)S, \tag{A9c}$$

with $\sigma_{\text{eff}} = [(V_p\sigma_e + V_e\sigma_p)/(V_eV_p)][\beta_S\tau_d/(\alpha_T\theta_*)]$.

b. Estimation of the parameters

In our choice of parameters, we deviate strongly from the values provided by Cessi (1994). First, Cessi (1994) assumes the same volume for the equatorial and polar oceanic boxes. This volume is given by the product of the typical depth $H = 4.5$ km, zonal extent $\delta_w = 300$ km, and meridional extent $L = 8250$ km. Here, we adopt the volume specifications used by Park (1999): $V = V_e + V_p = 5000\text{ km} \times 5000\text{ km} \times 4\text{ km}$ and $V_e \simeq 9V_p$, which is also in line with a Nordic seas surface of 2.5×10^6 km^2 indicated in Drange et al. (2005). Regarding the time scale τ_r we argue that the relaxation involves vertical heat transport within the oceanic boxes. Clearly, in a 4-km-deep ocean basin the temperature is a function of the depth. However, we cannot resolve the resulting temperature profile in our two-box framework. In particular, our boxes neglect the dynamics at the ocean's surface layer where complex processes like freezing and melting and high susceptibility to atmospheric forcing play an important role. We consider a depth of $D = 800$ m to estimate τ_r, because our model variable T_p shall reflect changes in the intermediate to deep Nordic seas temperatures (Sadatzki et al. 2020). Together with a typical vertical diffusivity of $\kappa_z = 1 \times 10^{-4}$ m^2 s^{-1} (e.g., Vettoretti et al. 2022) we obtain

$$\tau_r = \frac{D^2}{\kappa_z} = \frac{1000^2\text{ m}^2}{1 \times 10^{-4}\text{ m}^2\text{ s}^{-1}} = 203\text{ years}. \tag{A10}$$

To estimate the diffusive time scale, we use an ocean horizontal diffusivity of $\kappa_h = 1000$ m^2 s^{-1} (Cessi 1994), which yields

$$\tau_d = \frac{L^2}{\kappa_h} = 793\text{ years}, \tag{A11}$$

with $L = 5000$ km according to the volume specification.

Given that our polar oceanic box is meant to represent the Nordic seas, the advective time scale is given by the ratio between the box volume and the AMOC's volume transport into the Nordic seas. According to Vettoretti and Peltier (2015, Fig. 2) the AMOC inflow into the Nordic seas was around 3 Sverdrups (1 Sv $\equiv 1 \times 10^6$ m^3 s^{-1}) during stadials and

$$\tau_a = \frac{V/10}{3\text{ Sv}} = 106\text{ years} \tag{A12}$$

serves as a rough estimate for the advective time scale in our model.

Finally, for the atmospheric relaxation time scale we choose a value of $\tau_\theta = 55$ days, which ranges between synoptic and seasonal time scales. This choice guarantees that in the absence of sea ice the atmospheric gradient θ is determined to equal contributions by the oceanic temperature gradient T and the background gradient θ_0 as we will show later.

To compute the ratio between the heat capacities of the high-latitude oceanic and atmospheric boxes, we need to specify the volume of the polar atmosphere W_p. We identify the polar atmospheric box with a volume that extends from 60° to 80°N and from 45°W to 25°E. The height of the troposphere over this area is approximately 6 km such that

$$\begin{aligned} W_p &= \int_{-45°}^{25°} d\phi \int_{10°}^{25°} \sin(\theta) d\theta \int_{R_0}^{R_0+6\text{km}} r^2 dr \\ &= -\phi\Big|_{-45°}^{25°} \times \cos(\theta)\Big|_{10°}^{25°} \times 1/3r^3\Big|_{R_0}^{R_0+6\text{km}} \\ &\approx 23.3 \times 10^6\text{ km}^3, \end{aligned} \tag{A13}$$

where we have used the polar radius of Earth $R_0 = 6357$ km. The total heat capacity follows by multiplying the volume with a typical density of air $\rho_\theta = 1.2985 \times 1000^3$ kg km^{-3} and its specific heat capacity $c_\theta = 1035$ J kg^{-1} K^{-1}:

$$\lambda_p = \rho_\theta c_\theta W_p \approx 3 \times 10^{19}\text{ J K}^{-1}. \tag{A14}$$

For the ocean, the above specifications imply a volume of the polar box of

$$\begin{aligned} V_p &= V/10 = 5000\text{ km} \times 5000\text{ km} \times 4\text{ km} \times 10^{-1} \\ &= 10 \times 10^6\text{ km}^3, \end{aligned} \tag{A15}$$

yielding an oceanic heat capacity of

$$\Lambda_p = \rho_0 c_0 V_p \approx 4 \times 10^{22}\text{ J K}^{-1}, \tag{A16}$$

with the oceanic reference density of $\rho_0 = 1029 \times 1000^3$ kg km^{-3} and its specific heat capacity $c_0 = 3.9 \times 10^3$ J kg^{-1} K^{-1}. The ratio of atmospheric and oceanic heat capacities is thus given by $\Lambda_p/\lambda_p = 1323$. Dividing the atmospheric equation of motion by this ratio and introducing the time scale $\tau_{\text{atm}}\ \tau_d\lambda_p/\Lambda_p = 0.6$ years immediately reveals a clear time scale separation between atmosphere and ocean dynamics.

Finally, we need to specify the effective salinity forcing σ_{eff}. Typically, this value is considered a bifurcation parameter in applications of the Stommel model (Stommel 1961; Park 1999; Roberts and Saha 2017; Lohmann et al. 2021). Here we keep the value of σ_{eff} fixed at 0.7, which is on the lower end of the commonly considered parameter range.

In place of σ_{eff}, we vary τ_r, which will give rise to a similar bifurcation structure. We argue that the flux ϕ_p or equivalently the flux parameter γ_p is a function of the Nordic seas' sea ice cover which, if present, acts as an insulator between atmosphere and ocean. The value $\tau_r = 202$ years specified above shall correspond to ice free conditions. With sea ice being the fourth dynamical variable of our model, the rate $\gamma_p(I)$ and correspondingly τ_r is

subject to dynamic changes. This mechanism will be described in detail further below and for now we concentrate on the solutions of Eqs. (A9) in dependence on a variation of $\gamma_p \propto \tau_d/\tau_r$. For sake of readability, we introduce the parameters $\tau_{\text{atm}} = \tau_d\lambda_p/\Lambda_p \approx 0.6$, $\tau_{\text{ocean}} = \tau_d \approx 800$, $\Gamma = (\tau_d\lambda_p)/(\tau_\theta\Lambda_p) \approx 4$, $\gamma = \tau_d/\tau_r \approx 4$, and $\eta = \tau_d/\tau_a \approx 7.5$ and rewrite Eqs. (A9) as

$$\tau_{\text{atm}}\frac{d\theta}{dt} \approx -\Gamma(\theta - \theta_0) - \gamma(\theta - T), \tag{A17a}$$

$$\tau_{\text{ocean}}\frac{dT}{dt} \approx -\gamma(\theta - T) - (1 - \mu|S - T|)T, \tag{A17b}$$

$$\tau_{\text{ocean}}\frac{dS}{dt} \approx \sigma_{\text{eff}} - (1 - \mu|S - T|)S. \tag{A17c}$$

Let $q = T - S$ denote the nondimensionalized meridional density gradient. From $\psi = k\Delta\rho$ and $k = V_p/(\tau_a\rho_0\alpha_T\theta_*)$ it follows that

$$\psi = \frac{V_p}{\tau_a\rho_0\alpha_T\theta_*}\alpha_T\theta_*\rho_0 q = \frac{V_p}{\tau_a}q = \psi_0 q. \tag{A18}$$

So the nondimensional q indicates the strength of the AMOC in units of $\psi_0 = 3$ Sv. Since $|T - S|$ is generally less than 1, this will effectively yield unrealistically small values for the AMOC. Hence, the model is not self-consistent in the sense that assuming a typical value for the AMOC transport to estimate the time scale τ_{adv} implies that the modeled AMOC strength will always be less than the considered typical AMOC strength. However, since the available paleoclimate data only provide qualitative information on past AMOC changes, we correspondingly consider q as a qualitative indicator for the AMOC behavior attaching limited importance to quantitative correctness.

c. Dynamics of the extended Stommel model

We will later introduce explicit dependencies of θ_0 and γ on the temporarily varying background climate and the sea ice state, respectively. As a first step, we now discuss the dynamics of the extended Stommel model defined by Eqs. (A17) for a constant background and a prescribed mutual relaxation rate γ. Figure A1 shows the model's bifurcation diagram with γ acting as a bifurcation parameter. As the standard Stommel model, the extended model has two stable fixed point branches. For $1.4 < \gamma < 1.63$ the system is bistable with an unstable branch separating the two stable ones. The lower branch is associated with a weak mode of overturning (smaller $|q|$) while the upper branch represents a strong mode (larger $|q|$), with the former being salinity-driven ($S > T$) and the latter being temperature-driven ($T > S$). We note that the increase of q with increasing γ is stronger in the standard Stommel model because in the extended model a strengthening of the AMOC weakens the atmospheric temperature gradient and thus its own driving force.

Given the interpretation of the model variables established in the main text, with θ corresponding to Arctic atmospheric temperatures, T representing the Nordic seas' deep and intermediate water temperatures, and q indicating the AMOC strength, we can identify stadial and interstadial climate conditions with different configurations of the extended Stommel model. The atmosphere–ocean mutual temperature relaxation rate γ controls the state of the high-latitude climate (Fig. A1). Varying γ from low to high values yields qualitative changes in all three model variables that consistently match the changes of the true climate system observed between stadial and interstadial periods. Low values of $\gamma \lesssim 0.8$ are associated with a weak AMOC state (lower $|q|$ compared with the strong stable AMOC branch), cold polar atmosphere (large θ) and warm Nordic seas (small T), while high values of $\gamma \gtrsim 1.7$ reverse this configuration. This allows us to interpret the stable states of the extended Stommel model at low and high γ as stadial and interstadial states, respectively.

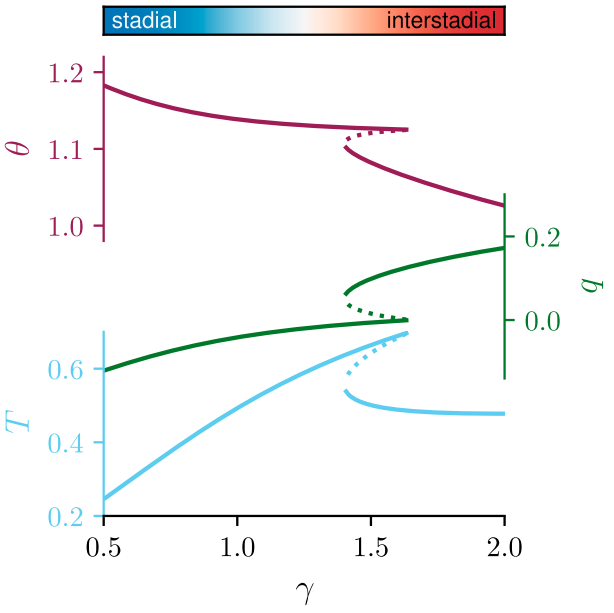

FIG. A1. Bifurcation diagram of the extended Stommel model defined by Eq. (A17). The mutual relaxation rate γ acts as a control parameter with two bifurcations occurring at $\gamma_{c1} \approx 1.4$ and $\gamma_{c2} \approx 1.63$. Solid (dashed) lines represent stable (unstable) branches. The atmospheric meridional temperature gradient θ declines with increasing heat exchange rate γ due to the action of the ocean on the atmosphere. The stable branch of the model that is associated with higher γ is commonly referred to as the strong mode (temperature driven), while the stable branch associated with lower γ is called the weak mode (salinity driven). For low $\gamma < 0.8$, all model variables assume a stadial configuration, while for $\gamma > 1.7$, they assume an interstadial configuration. Here, the atmospheric background climate is set to $\theta_0 = 1.3$ and all other parameters are as given in Table 1 in the main text.

Although higher values of γ entail enhanced oceanic northward heat transport, the Nordic seas are colder in this configuration because of the stronger release of heat into the atmosphere. In the stadial state (small values of γ) the model shows sustained northward heat transport provided by the salinity-driven weak AMOC. However, with the corresponding smaller atmosphere–ocean heat flux (smaller γ)

even a reduced northward heat transport warms the northern ocean as it hardly loses any heat to the atmosphere. This model behavior is in line with the findings by Rasmussen and Thomsen (2004), Dokken et al. (2013), and Ezat et al. (2014), who report a sustained warm water inflow into the Nordic seas at intermediate depth during stadials. Subsurface warming at high latitudes was also reproduced by complex modeling studies (Vettoretti and Peltier 2018; Kuniyoshi et al. 2022).

d. Sea ice component

The sea ice variable I represents the sea ice cover in the polar box (i.e., in the Nordic seas). Acting as an insulator, the sea ice controls the heat flux ϕ_p between the polar atmosphere and ocean (Dokken et al. 2013; Boers et al. 2018). In the concise model formulation [Eqs. (A17)], this control may effectively be expressed by introducing an explicit dependency of the model parameter γ on the sea ice variable I. To model the sea ice dynamics, we adopt the seasonally averaged version of the Eisenman (2012) sea ice model introduced by Lohmann et al. (2021):

$$\dot{I} = \Delta \tanh\left(\frac{I}{h}\right) - R_0 H(I)\, I + L - BI, \tag{A19}$$

where $H(I)$ denotes the Heaviside function. The first term represents the ice-albedo feedback to the incoming solar shortwave radiation. The sea ice transport, which is absent in open ocean conditions ($I < 0$), is controlled by R_0. The term $L - BI$ describes the change of sea ice due to the net outgoing longwave radiation (OLR) according to a linearized Stefan–Boltzmann law. The incoming longwave radiation depends on the atmospheric temperature θ. For the derivation of the nondimensionalized equation, please see Eisenman (2012).

To incorporate dynamic changes of the polar atmospheric temperature in Eq. (A19) and to couple the sea ice model with the extended Stommel model, we assume a linear relationship between the net incoming (or outgoing) longwave radiation and the atmospheric temperature and write

$$L = L_0 + L_1(\theta - \theta_*), \tag{A20}$$

where $\theta - \theta_*$ denotes deviations from the typical atmospheric temperature gradient. Since larger θ corresponds to a colder polar atmosphere with positive effect on the sea ice growth, L_1 is positive. Inserting Eq. (A20) into Eq. (A19) finally leads to our sea ice model given by Eq. (6) in the main text

$$\tau_{\text{ice}}\dot{I} = \Delta \tanh\left(\frac{I}{h}\right) - R_0 H(I) I - L_0 + L_1\theta - L_2 I, \tag{A21}$$

yet without the stochastic forcing ξ_t. We ignore influences of the intermediate to deep ocean temperatures on the sea ice formation and melt and instead assume that the ocean's surface layer is governed by the atmospheric temperatures.

Notice that the extended Stommel model is formulated such that energy is conserved. Incorporating the sea ice model into the Stommel model while respecting conservation of energy would require resolving different layers of the polar ocean box and in particular the fluxes into and out of the surface layer and the sea ice itself. Since the heat capacity of the ocean's surface layer is relatively small compared to the heat capacities of the considered oceanic and atmospheric boxes, we may ignore the exact amount of energy that enters and leaves this layer.

In the original version of the Eisenman (2012) model the sea ice variable I describes the ice thickness over an isolated ocean column of small spatial extent with horizontally homogeneous temperature. In particular, negative I corresponds to ice-free conditions (Eisenman 2012). Given the large spatial extent of the polar box, the homogeneity assumption does not hold in our application. Instead, we interpret the variable I as a stylized representation of the sea ice over the Nordic seas and its impact on the atmosphere–ocean heat flux. In this context, we introduce the time scale τ_{ice} to express that I reflects slow changes of the annually averaged total sea ice volume instead of the fairly rapid dynamics of growing or melting sea ice at an individual point in space. For given climatic conditions sea ice equilibrates fairly rapidly, meaning that it either forms or melts in a single season. Multiyear sea ice does usually not exceed an age of roughly 10 years setting an upper bound on typical relaxation time scale of sea ice with respect to changing climatic conditions at a given location. The much larger time scale of $\tau_{\text{ice}} = 200$ years chosen for our study corresponds to the time scale of changes in the multiyear sea ice edge.

As previously mentioned, sea ice insulates the atmosphere and the ocean from one another and hence controls their mutual heat flux. Based on our altered interpretation of the sea ice variable I, we model the effect of the sea ice on the ocean–atmosphere heat flux in form of a hyperbolic tangent with saturation toward high and low values of sea ice:

$$\gamma(I) = \gamma_0 + \frac{\Delta\gamma}{2}\left\{\tanh\left[\frac{-(I - I_0)}{\omega}\right] + 1\right\}. \tag{A22}$$

This yields a heat flux $\phi_p \propto \gamma(I)(T - \theta)$ that in turn controls the mutual atmosphere–ocean relaxation in terms of temperatures. The parameters γ_0 and $\gamma_0 + \Delta\gamma$ in Eq. (A22) define the mutual relaxation rate at maximum ice cover and open ocean conditions, respectively, and ω moderates the steepness of the rate's decline with increasing sea ice thickness I. Shifting the hyperbolic tangent along the sea ice axis by setting $I_0 = -0.5$ yields an already substantially reduced heat flux at intermediate sea ice cover ($I = 0$; cf. Fig. A2). At maximum sea ice cover the heat exchange between the high-latitude ocean and atmosphere is considered to be (almost) shut off. At low latitudes, the heat flux is unaffected by the sea ice. As explained in the derivation of the extended Stommel model, the term $\gamma(I)(T - \theta)$ is dominated by the heat flux between the polar ocean and atmosphere as we have assumed $\theta_e \sim T_e$. Thus, we choose a relatively small $\gamma_0 = 0.5$ which reflects a substantially reduced total atmosphere–ocean heat flux at maximum sea ice cover. The parameters for the sea ice model were adopted from Eisenman (2012) and

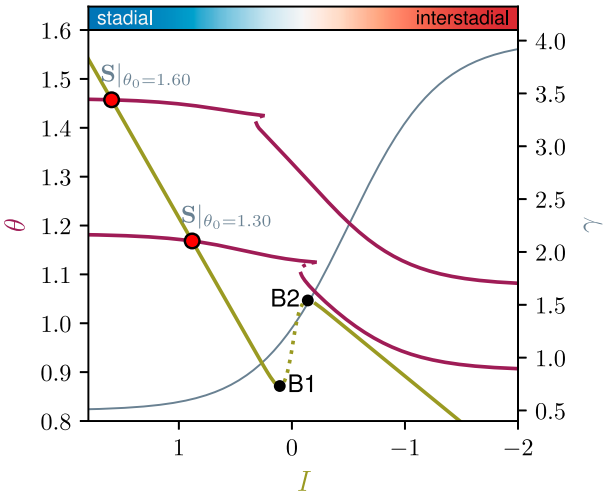

FIG. A2. Nullcline of the seasonally averaged sea ice I (olive) together with the nullcline of the Stommel atmosphere θ (wine). Due to the ice albedo feedback the sea ice model features a bistable region where an ice-rich and a low-ice solution coexist. The difference in the slope of the two stable branches is controlled by the strength of the sea ice export R_0. The lower θ-nullcline is the same as in Fig. A1 with $\theta_0 = 1.3$ upon using the transformation $\gamma = \gamma(I)$ given by Eq. (A22). The upper θ-nullcline results from setting $\theta_0 = 1.6$. The mutual relaxation rate $\gamma(I)$ as a function of the sea ice is shown in light gray on the right ordinate. Intersections of the θ and I nullclines define fixed points of the entire coupled system defined by Eqs. (A17) and (A21). Larger atmospheric backgrounds θ_0 yield more pronounced stadial conditions with colder Arctic atmosphere and larger sea ice cover.

Lohmann et al. (2021). Only the newly introduced L_0 and L_1 were tuned by hand to align the model's DO cycle shape with that observed in the NGRIP record.

e. Dynamics of the coupled atmosphere–ocean–sea ice model

We now examine the joint bifurcation structure of the sea ice model and the atmospheric temperature θ in the deterministic setting—that is, we assess the nullclines of Eqs. (A17) and (A21) (see the main text for our working definition of the *nullclines*). Our sea ice model features a double fold bifurcation with respect to θ (Fig. A2). The associated bistability is an effect of the ice–albedo feedback. The bifurcation points are given by B1 = (θ = 0.83, I = 0.11) and B2 = (θ = 1.06, I = −0.14). Intersections of the sea ice's and the atmosphere's nullclines constitute fixed points of the full coupled system. The stable fixed points that correspond to the two climate background states $\theta_0 = 1.3$ and $\theta_0 = 1.6$ are ($\theta_s \approx 1.17$, $I_s \sim 0.88$) and ($\theta_s \approx 1.45$, $I_s \sim 1.59$), respectively, and represent stadial climate states with large sea ice cover and cold temperatures over Greenland (red dots in Fig. A2). Note that larger atmospheric background gradients yield a more severe stadial climate with larger I_s and θ_s. The corresponding stadial fixed points in the ocean model, i.e., in Eqs. (A17), are $T_s \approx 0.3$ and $T_s \approx 0.36$, implying relatively warm Nordic seas. Moreover, the AMOC strength ($q_s \sim -0.1$ and $q_s \sim -0.08$) is negative and thus salinity driven and weak.

A key feature of the bifurcation diagram is the proximity of the low-ice stable branch of the sea ice nullcline and the strong-mode stable branch of the θ nullcline around $I \approx -0.4$. The closer the nullclines are to each other, the slower the deterministic dynamics in nearby regions of the state space. Their distance is controlled by the atmospheric climate background θ_0 and decreases with decreasing θ_0 provided that $\theta_0 > 1.275$. If the nullclines are sufficiently close, once the system enters this region of the state space, the dynamics allows for prolonged periods in which I and θ do not vary much, giving rise to what we term a metastable state. It is the existence of this transient metastable state that allows us to model prolonged interstadials typical for DO cycles.

To bring the system close to the metastable state, we require sufficiently large perturbations. In our model these are provided by substantial stochastic sea ice removals that reactivate the ocean–atmosphere interaction and thereby trigger temporary state-space excursions into the interstadial regime. This is achieved by introducing a non-Gaussian intermittent stochastic process that acts as a forcing on the sea ice and is capable of inducing the required large abrupt sea ice removal.

REFERENCES

Berben, S. M. P., T. M. Dokken, P. M. Abbott, E. Cook, H. Sadatzki, M. H. Simon, and E. Jansen, 2020: Independent tephrochronological evidence for rapid and synchronous oceanic and atmospheric temperature rises over the Greenland stadial-interstadial transitions between ca. 32 and 40 ka b2k. *Quat. Sci. Rev.*, **236**, 106277, https://doi.org/10.1016/j.quascirev.2020.106277.

Boers, N., M. Ghil, and D. D. Rousseau, 2018: Ocean circulation, ice shelf, and sea ice interactions explain Dansgaard–Oeschger cycles. *Proc. Natl. Acad. Sci. USA*, **115**, E11 005–E11 014, https://doi.org/10.1073/pnas.1802573115.

Broecker, W. S., D. M. Peteet, and D. Rind, 1985: Does the ocean–atmosphere system have more than one stable mode of operation? *Nature*, **315**, 21–26, https://doi.org/10.1038/315021a0.

——, G. Bond, M. Klas, G. Bonani, and W. Wolfli, 1990: A salt oscillator in the glacial Atlantic? 1. The concept. *Paleoceanography*, **5**, 469–477, https://doi.org/10.1029/PA005i004p00469.

Cessi, P., 1994: A simple box model of stochastically forced thermohaline flow. *J. Phys. Oceanogr.*, **24**, 1911–1920, https://doi.org/10.1175/1520-0485(1994)024<1911:ASBMOS>2.0.CO;2.

Cheng, H., and Coauthors, 2013: Climate change patterns in Amazonia and biodiversity. *Nat. Commun.*, **4**, 1411, https://doi.org/10.1038/ncomms2415.

Clark, P. U., and Coauthors, 2009: The last glacial maximum. *Science*, **325**, 710–714, https://doi.org/10.1126/science.1172873.

Corrick, E. C., and Coauthors, 2020: Synchronous timing of abrupt climate changes during the last glacial period. *Science*, **369**, 963–969, https://doi.org/10.1126/science.aay5538.

Dansgaard, W., H. B. Clausen, N. Gundestrup, C. U. Hammer, S. F. Johnsen, P. M. Kristinsdottir, and N. Reeh, 1982: A new Greenland deep ice core. *Science*, **218**, 1273–1277, https://doi.org/10.1126/science.218.4579.1273.

——, S. J. Johnsen, H. B. Clausen, D. Dahl-Jensen, N. Gundestrup, C. U. Hammer, and H. Oeschger, 1984: North Atlantic climatic

oscillations revealed by deep Greenland ice cores. *Climate Processes and Climate Sensitivity*, J. Hansen and T. Takahashi, Eds., Amer. Geophys. Union, 288–298, https://doi.org/10.1029/GM029p0288.

——, and Coauthors, 1993: Evidence for general instability of past climate from a 250-kyr ice-core record. *Nature*, **364**, 218–220, https://doi.org/10.1038/364218a0.

De Boer, A. M., A. Gnanadesikan, N. R. Edwards, and A. J. Watson, 2010: Meridional density gradients do not control the Atlantic overturning circulation. *J. Phys. Oceanogr.*, **40**, 368–380, https://doi.org/10.1175/2009JPO4200.1.

Ditlevsen, P. D., 1999: Observation of α-stable noise induced millennial climate changes from an ice-core record. *Geophys. Res. Lett.*, **26**, 1441–1444, https://doi.org/10.1029/1999GL900252.

——, M. S. Kristensen, and K. K. Andersen, 2005: The recurrence time of Dansgaard–Oeschger events and limits on the possible periodic component. *J. Climate*, **18**, 2594–2603, https://doi.org/10.1175/JCLI3437.1.

——, K. K. Andersen, and A. Svensson, 2007: The DO-climate events are probably noise induced: Statistical investigation of the claimed 1470 years cycle. *Climate Past*, **3**, 129–134, https://doi.org/10.5194/cp-3-129-2007.

Dokken, T. M., K. H. Nisancioglu, C. Li, D. S. Battisti, and C. Kissel, 2013: Dansgaard-Oeschger cycles: Interactions between ocean and sea ice intrinsic to the Nordic seas. *Paleoceanography*, **28**, 491–502, https://doi.org/10.1002/palo.20042.

Drange, H., and Coauthors, 2005: The Nordic seas: An overview. *The Nordic Seas: An Integrated Perspective*, H. Drange et al., Eds., Amer. Geophys. Union, 1–10, https://doi.org/10.1029/158GM02.

Drijfhout, S., E. Gleeson, H. A. Dijkstra, and V. Livina, 2013: Spontaneous abrupt climate change due to an atmospheric blocking–sea-ice–ocean feedback in an unforced climate model simulation. *Proc. Natl. Acad. Sci. USA*, **110**, 19 713–19 718, https://doi.org/10.1073/pnas.1304912110.

Eisenman, I., 2012: Factors controlling the bifurcation structure of sea ice retreat. *J. Geophys. Res.*, **117**, D01111, https://doi.org/10.1029/2011JD016164.

Ezat, M. M., T. L. Rasmussen, and J. Groeneveld, 2014: Persistent intermediate water warming during cold stadials in the southeastern Nordic seas during the past 65 k.y. *Geology*, **42**, 663–666, https://doi.org/10.1130/G35579.1.

Fischer, H., M.-L. Siggaard-Andersen, U. Ruth, R. Röthlisberger, and E. Wolff, 2007: Glacial/interglacial changes in mineral dust and sea-salt records in polar ice cores: Sources, transport, and deposition. *Rev. Geophys.*, **45**, RG1002, https://doi.org/10.1029/2005RG000192.

FitzHugh, R., 1961: Impulses and physiological states in theoretical models of nerve membrane. *Biophys. J.*, **1**, 445–466, https://doi.org/10.1016/S0006-3495(61)86902-6.

Fuhrer, K., A. Neftel, M. Anklin, and V. Maggi, 1993: Continuous measurements of hydrogen peroxide, formaldehyde, calcium and ammonium concentrations along the new grip ice core from summit, Central Greenland. *Atmos. Environ.*, **27A**, 1873–1880, https://doi.org/10.1016/0960-1686(93)90292-7.

Ganopolski, A., and S. Rahmstorf, 2001: Rapid changes of glacial climate simulated in a coupled climate model. *Nature*, **409**, 153–158, https://doi.org/10.1038/35051500.

——, and ——, 2002: Abrupt glacial climate changes due to stochastic resonance. *Phys. Rev. Lett.*, **88**, 038501, https://doi.org/10.1103/PhysRevLett.88.038501.

Gnanadesikan, A., 1999: A simple predictive model for the structure of the oceanic pycnocline. *Science*, **283**, 2077–2079, https://doi.org/10.1126/science.283.5410.2077.

Gottschalk, J., L. C. Skinner, S. Misra, C. Waelbroeck, L. Menviel, and A. Timmermann, 2015: Abrupt changes in the southern extent of North Atlantic deep water during Dansgaard–Oeschger events. *Nat. Geosci.*, **8**, 950–954, https://doi.org/10.1038/ngeo2558.

Gottwald, G. A., 2021: A model for Dansgaard–Oeschger events and millennial-scale abrupt climate change without external forcing. *Climate Dyn.*, **56**, 227–243, https://doi.org/10.1007/s00382-020-05476-z.

——, and I. Melbourne, 2013a: A Huygens principle for diffusion and anomalous diffusion in spatially extended systems. *Proc. Natl. Acad. Sci. USA*, **110**, 8411–8416, https://doi.org/10.1073/pnas.1217926110.

——, and ——, 2013b: Homogenization for deterministic maps and multiplicative noise. *Proc. Roy. Soc.*, **469A**, 20130201, https://doi.org/10.1098/rspa.2013.0201.

——, D. T. Crommelin, and C. L. E. Franzke, 2017: Stochastic climate theory. *Nonlinear and Stochastic Climate Dynamics*, C. L. E. Franzke and T. J. O'Kane, Eds., Cambridge University Press, 209–240, https://doi.org/10.1017/9781316339251.

Hasselmann, K., 1976: Stochastic climate models: Part I. Theory. *Tellus*, **28A**, 473–485, https://doi.org/10.1111/j.2153-3490.1976.tb00696.x.

Henry, L. G., J. F. McManus, W. B. Curry, N. L. Roberts, A. M. Piotrowski, and L. D. Keigwin, 2016: North Atlantic Ocean circulation and abrupt climate change during the last glaciation. *Science*, **353**, 470–474, https://doi.org/10.1126/science.aaf5529.

Hines, S. K. V., A. F. Thompson, and J. F. Adkins, 2019: The role of the southern ocean in abrupt transitions and hysteresis in glacial ocean circulation. *Paleoceanogr. Paleoclimatol.*, **34**, 490–510, https://doi.org/10.1029/2018PA003415.

Hoff, U., T. L. Rasmussen, R. Stein, M. M. Ezat, and K. Fahl, 2016: Sea ice and millennial-scale climate variability in the Nordic seas 90 kyr ago to present. *Nat. Commun.*, **7**, 12247, https://doi.org/10.1038/ncomms12247.

Huber, C., and Coauthors, 2006: Isotope calibrated Greenland temperature record over Marine Isotope Stage 3 and its relation to CH4. *Earth Planet. Sci. Lett.*, **243**, 504–519, https://doi.org/10.1016/j.epsl.2006.01.002.

Jensen, M. F., J. Nilsson, and K. H. Nisancioglu, 2016: The interaction between sea ice and salinity-dominated ocean circulation: Implications for halocline stability and rapid changes of sea ice cover. *Climate Dyn.*, **47**, 3301–3317, https://doi.org/10.1007/s00382-016-3027-5.

Johnsen, S. J., and Coauthors, 1992: Irregular glacial interstadials recorded in a new Greenland ice core. *Nature*, **359**, 311–313, https://doi.org/10.1038/359311a0.

——, and Coauthors, 2001: Oxygen isotope and palaeotemperature records from six Greenland ice-core stations: Camp century, Dye-3, GRIP, GISP2, Renland and NorthGRIP. *J. Quat. Sci.*, **16**, 299–307, https://doi.org/10.1002/jqs.622.

Jouzel, J., and Coauthors, 1997: Validity of the temperature reconstruction from water isotopes in ice cores. *J. Geophys. Res.*, **102**, 26 471–26 487, https://doi.org/10.1029/97JC01283.

Kanner, L. C., S. J. Burns, H. Cheng, and R. L. Edwards, 2012: High-latitude forcing of the South American summer monsoon during the last glacial. *Science*, **335**, 570–573, https://doi.org/10.1126/science.1213397.

Kindler, P., M. Guillevic, M. Baumgartner, J. Schwander, A. Landais, and M. Leuenberger, 2014: Temperature reconstruction from 10 to 120 kyr b2k from the NGRIP ice core. *Climate Past*, **10**, 887–902, https://doi.org/10.5194/cp-10-887-2014.

Kleppin, H., M. Jochum, B. Otto-Bliesner, C. A. Shields, and S. Yeager, 2015: Stochastic atmospheric forcing as a cause of Greenland climate transitions. *J. Climate*, **28**, 7741–7763, https://doi.org/10.1175/JCLI-D-14-00728.1.

Kuniyoshi, Y., A. Abe-Ouchi, S. Sherriff-Tadano, W.-L. Chan, and F. Saito, 2022: Effect of climatic precession on Dansgaard-Oeschger-like oscillations. *Geophys. Res. Lett.*, **49**, e2021GL095695, https://doi.org/10.1029/2021GL095695.

Kwasniok, F., 2013: Analysis and modelling of glacial climate transitions using simple dynamical systems. *Philos. Trans. Roy. Soc.*, **A371**, 20110472, https://doi.org/10.1098/rsta.2011.0472.

Landais, A., J. Jouzel, V. Masson-Delmotte, and N. Caillon, 2005: Large temperature variations over rapid climatic events in Greenland: A method based on air isotopic measurements. *C. R. Geosci.*, **337**, 947–956, https://doi.org/10.1016/j.crte.2005.04.003.

Li, C., and A. Born, 2019: Coupled atmosphere-ice-ocean dynamics in Dansgaard-Oeschger events. *Quat. Sci. Rev.*, **203** (5020), 1–20, https://doi.org/10.1016/j.quascirev.2018.10.031.

——, D. S. Battisti, D. P. Schrag, and E. Tziperman, 2005: Abrupt climate shifts in Greenland due to displacements of the sea ice edge. *Geophys. Res. Lett.*, **32**, L19702, https://doi.org/10.1029/2005GL023492.

——, ——, and C. M. Bitz, 2010: Can North Atlantic sea ice anomalies account for Dansgaard–Oeschger climate signals? *J. Climate*, **23**, 5457–5475, https://doi.org/10.1175/2010JCLI3409.1.

Lisiecki, L. E., and M. E. Raymo, 2005: A Pliocene-Pleistocene stack of 57 globally distributed benthic δ^{18}O records. *Paleoceanography*, **20**, PA1003, https://doi.org/10.1029/2004PA001071.

Livina, V. N., F. Kwasniok, and T. M. Lenton, 2010: Potential analysis reveals changing number of climate states during the last 60 kyr. *Climate Past*, **6**, 77–82, https://doi.org/10.5194/cp-6-77-2010.

Lohmann, J., and P. D. Ditlevsen, 2018: Random and externally controlled occurrences of Dansgaard–Oeschger events. *Climate Past*, **14**, 609–617, https://doi.org/10.5194/cp-14-609-2018.

——, and ——, 2019: Objective extraction and analysis of statistical features of Dansgaard–Oeschger events. *Climate Past*, **15**, 1771–1792, https://doi.org/10.5194/cp-15-1771-2019.

——, and A. Svensson, 2022: Ice core evidence for major volcanic eruptions at the onset of Dansgaard–Oeschger warming events. *Climate Past*, **18**, 2021–2043, https://doi.org/10.5194/cp-18-2021-2022.

——, D. Castellana, P. D. Ditlevsen, and H. A. Dijkstra, 2021: Abrupt climate change as a rate-dependent cascading tipping point. *Earth Syst. Dyn.*, **12**, 819–835, https://doi.org/10.5194/esd-12-819-2021.

Lynch-Stieglitz, J., 2017: The Atlantic meridional overturning circulation and abrupt climate change. *Annu. Rev. Mar. Sci.*, **9**, 83–104, https://doi.org/10.1146/annurev-marine-010816-060415.

Malmierca-Vallet, I., L. C. Sime, and D–O community members, 2023: Dansgaard–Oeschger events in climate models: Review and baseline marine isotope stage 3 (MIS3) protocol. *Climate Past*, **19**, 915–942, https://doi.org/10.5194/cp-19-915-2023.

Masson-Delmotte, V., and Coauthors, 2006: Past and future polar amplification of climate change: Climate model intercomparisons and ice-core constraints. *Climate Dyn.*, **26**, 513–529, https://doi.org/10.1007/s00382-005-0081-9.

Menviel, L., A. Timmermann, T. Friedrich, and M. H. England, 2014: Hindcasting the continuum of Dansgaard–Oeschger variability: Mechanisms, patterns and timing. *Climate Past*, **10**, 63–77, https://doi.org/10.5194/cp-10-63-2014.

——, L. C. Skinner, L. Tarasov, and P. C. Tzedakis, 2020: An ice–climate oscillatory framework for Dansgaard–Oeschger cycles. *Nat. Rev. Earth Environ.*, **1**, 677–693, https://doi.org/10.1038/s43017-020-00106-y.

Mitsui, T., and M. Crucifix, 2017: Influence of external forcings on abrupt millennial-scale climate changes: A statistical modelling study. *Climate Dyn.*, **48**, 2729–2749, https://doi.org/10.1007/s00382-016-3235-z.

Nagumo, J., S. Arimoto, and S. Yoshizawa, 1962: An active pulse transmission line simulating nerve axon. *Proc. IRE*, **50**, 2061–2070, https://doi.org/10.1109/JRPROC.1962.288235.

Nikurashin, M., and G. Vallis, 2011: A theory of deep stratification and overturning circulation in the ocean. *J. Phys. Oceanogr.*, **41**, 485–502, https://doi.org/10.1175/2010JPO4529.1.

North Greenland Ice Core Project Members, 2004: High-resolution record of Northern Hemisphere climate extending into the last interglacial period. *Nature*, **431**, 147–151, https://doi.org/10.1038/nature02805.

Park, Y.-G., 1999: The stability of thermohaline circulation in a two-box model. *J. Phys. Oceanogr.*, **29**, 3101–3110, https://doi.org/10.1175/1520-0485(1999)029<3101:TSOTCI>2.0.CO;2.

Petersen, S. V., D. P. Schrag, and P. U. Clark, 2013: A new mechanism for Dansgaard-Oeschger cycles. *Paleoceanography*, **28**, 24–30, https://doi.org/10.1029/2012PA002364.

Rasmussen, S. O., and Coauthors, 2014: A stratigraphic framework for abrupt climatic changes during the last glacial period based on three synchronized Greenland ice-core records: Refining and extending the INTIMATE event stratigraphy. *Quat. Sci. Rev.*, **106**, 14–28, https://doi.org/10.1016/j.quascirev.2014.09.007.

Rasmussen, T. L., and E. Thomsen, 2004: The role of the North Atlantic drift in the millennial timescale glacial climate fluctuations. *Palaeogeogr. Palaeoclimatol. Palaeoecol.*, **210**, 101–116, https://doi.org/10.1016/j.palaeo.2004.04.005.

——, ——, L. Labeyrie, and T. C. E. van Weering, 1996a: Circulation changes in the Faeroe-Shetland channel correlating with cold events during the last glacial period (58-10 ka). *Geology*, **24**, 937–940, https://doi.org/10.1130/0091-7613(1996)024<0937:CCITFS>2.3.CO;2.

——, ——, T. C. E. van Weering, and L. Labeyrie, 1996b: Rapid changes in surface and deep water conditions at the Faeroe Margin during the last 58,000 years. *Paleoceanogr. Paleoclimatol.*, **11**, 757–771, https://doi.org/10.1029/96PA02618.

Rial, J. A., and R. Saha, 2011: Modeling abrupt climate change as the interaction between sea ice extent and mean ocean temperature under orbital insolation forcing. *Abrupt Climate Change: Mechanisms, Patterns, and Impacts*, H. Rashid, L. Polyak, and E. Mosley-Thompson, Eds., Amer. Geophys. Union, 57–74, https://doi.org/10.1029/2010GM001027.

Roberts, A., and R. Saha, 2017: Relaxation oscillations in an idealized ocean circulation model. *Climate Dyn.*, **48**, 2123–2134, https://doi.org/10.1007/s00382-016-3195-3.

Ruth, U., and Coauthors, 2007: Ice core evidence for a very tight link between North Atlantic and East Asian glacial climate. *Geophys. Res. Lett.*, **34**, L03706, https://doi.org/10.1029/2006GL027876.

Sadatzki, H., and Coauthors, 2019: Sea ice variability in the southern Norwegian sea during glacial Dansgaard-Oeschger

climate cycles. *Sci. Adv.*, **5**, eaau6174, https://doi.org/10.1126/sciadv.aau6174.

——, and Coauthors, 2020: Rapid reductions and millennial-scale variability in Nordic seas sea ice cover during abrupt glacial climate changes. *Proc. Natl. Acad. Sci. USA*, **117**, 29 478–29 486, https://doi.org/10.1073/pnas.2005849117.

Schüpbach, S., and Coauthors, 2018: Greenland records of aerosol source and atmospheric lifetime changes from the Eemian to the Holocene. *Nat. Commun.*, **9**, 1476, https://doi.org/10.1038/s41467-018-03924-3.

Seierstad, I. K., and Coauthors, 2014: Consistently dated records from the Greenland GRIP, GISP2 and NGRIP ice cores for the past 104ka reveal regional millennial-scale $\delta^{18}O$ gradients with possible Heinrich event imprint. *Quat. Sci. Rev.*, **106**, 29–46, https://doi.org/10.1016/j.quascirev.2014.10.032.

Singh, H. A., D. S. Battisti, and C. M. Bitz, 2014: A heuristic model of Dansgaard–Oeschger cycles. Part I: Description, results, and sensitivity studies. *J. Climate*, **27**, 4337–4358, https://doi.org/10.1175/JCLI-D-12-00672.1.

Stommel, H., 1961: Thermohaline convection with two stable regimes of flow. *Tellus*, **13A**, 224–230, https://doi.org/10.3402/tellusa.v13i2.9491.

Thompson, A. F., S. K. Hines, and J. F. Adkins, 2019: A Southern Ocean mechanism for the interhemispheric coupling and phasing of the bipolar seesaw. *J. Climate*, **32**, 4347–4365, https://doi.org/10.1175/JCLI-D-18-0621.1.

Timmermann, A., and G. Lohmann, 2000: Noise-induced transitions in a simplified model of the thermohaline circulation. *J. Phys. Oceanogr.*, **30**, 1891–1900, https://doi.org/10.1175/1520-0485(2000) 030<1891:NITIAS>2.0.CO;2.

——, H. Gildor, M. Schulz, and E. Tziperman, 2003: Coherent resonant millennial-scale climate oscillations triggered by massive meltwater pulses. *J. Climate*, **16**, 2569–2585, https://doi.org/10.1175/1520-0442(2003)016<2569:CRMCOT>2.0.CO;2.

Vettoretti, G., and W. R. Peltier, 2015: Interhemispheric air temperature phase relationships in the nonlinear Dansgaard-Oeschger oscillation. *Geophys. Res. Lett.*, **42**, 1180–1189, https://doi.org/10.1002/2014GL062898.

——, and ——, 2018: Fast physics and slow physics in the nonlinear Dansgaard–Oeschger relaxation oscillation. *J. Climate*, **31**, 3423–3449, https://doi.org/10.1175/JCLI-D-17-0559.1.

——, P. Ditlevsen, M. Jochum, and S. O. Rasmussen, 2022: Atmospheric CO_2 control of spontaneous millennial-scale ice age climate oscillations. *Nat. Geosci.*, **15**, 300–306, https://doi.org/10.1038/s41561-022-00920-7.

Voelker, A. H. L., 2002: Global distribution of centennial-scale records for marine isotope stage (MIS) 3: A database. *Quat. Sci. Rev.*, **21**, 1185–1212, https://doi.org/10.1016/S0277-3791(01)00139-1.

Wang, Y. J., H. Cheng, R. L. Edwards, Z. S. An, J. Y. Wu, C.-C. Shen, and J. A. Dorale, 2001: A high-resolution absolute-dated late Pleistocene monsoon record from Hulu Cave, China. *Science*, **294**, 2345–2348, https://doi.org/10.1126/science.1064618.

Weijer, W., and Coauthors, 2019: Stability of the Atlantic meridional overturning circulation: A review and synthesis. *J. Geophys. Res. Oceans*, **124**, 5336–5375, https://doi.org/10.1029/2019JC015083.

Yang, H., K. Wang, H. Dai, Y. Wang, and Q. Li, 2016: Wind effect on the Atlantic meridional overturning circulation via sea ice and vertical diffusion. *Climate Dyn.*, **46**, 3387–3403, https://doi.org/10.1007/s00382-015-2774-z.

Zhang, X., G. Lohmann, G. Knorr, and C. Purcell, 2014: Abrupt glacial climate shifts controlled by ice sheet changes. *Nature*, **512**, 290–294, https://doi.org/10.1038/nature13592.

——, S. Barker, G. Knorr, G. Lohmann, R. Drysdale, Y. Sun, D. Hodell, and F. Chen, 2021: Direct astronomical influence on abrupt climate variability. *Nat. Geosci.*, **14**, 819–826, https://doi.org/10.1038/s41561-021-00846-6.

Zhang, Y., and Coauthors, 2017: Different precipitation patterns across tropical South America during Heinrich and Dansgaard-Oeschger stadials. *Quat. Sci. Rev.*, **177**, 1–9, https://doi.org/10.1016/j.quascirev.2017.10.012.